# Neutrino fluxes from constrained minimal supersymmetric standard model lightest supersymmetric particle annihilations in the Sun

John Ellis,[1,*] Keith A. Olive,[2,†] Christopher Savage,[3,‡] and Vassilis C. Spanos[4,§]

[1]*TH Division, Physics Department, CERN, 1211 Geneva 23, Switzerland*
[2]*William I. Fine Theoretical Physics Institute, School of Physics and Astronomy, University of Minnesota, Minneapolis, Minnesota 55455, USA*
[3]*The Oskar Klein Centre for Cosmoparticle Physics, Department of Physics, Stockholm University, AlbaNova, SE-10691 Stockholm, Sweden*
[4]*Department of Physics, University of Patras, GR-26500 Patras, Greece*
(Received 18 December 2009; published 6 April 2010)

We evaluate the neutrino fluxes to be expected from neutralino lightest supersymmetric particle (LSP) annihilations inside the Sun, within the minimal supersymmetric extension of the standard model with supersymmetry-breaking scalar and gaugino masses constrained to be universal at the grand unified theory scale [the constrained minimal supersymmetric standard model (CMSSM)]. We find that there are large regions of typical CMSSM $(m_{1/2}, m_0)$ planes where the LSP density inside the Sun is not in equilibrium, so that the annihilation rate may be far below the capture rate. We show that neutrino fluxes are dependent on the solar model at the 20% level, and adopt the AGSS09 model of Serenelli *et al.* for our detailed studies. We find that there are large regions of the CMSSM $(m_{1/2}, m_0)$ planes where the capture rate is not dominated by spin-dependent LSP-proton scattering, e.g., at large $m_{1/2}$ along the CMSSM coannihilation strip. We calculate neutrino fluxes above various threshold energies for points along the coannihilation/rapid-annihilation and focus-point strips where the CMSSM yields the correct cosmological relic density for $\tan\beta = 10$ and 55 for $\mu > 0$, exploring their sensitivities to uncertainties in the spin-dependent and -independent scattering matrix elements. We also present detailed neutrino spectra for four benchmark models that illustrate generic possibilities within the CMSSM. Scanning the cosmologically favored parts of the parameter space of the CMSSM, we find that the IceCube/DeepCore detector can probe at best only parts of this parameter space, notably the focus-point region and possibly also at the low-mass tip of the coannihilation strip.

## I. INTRODUCTION

The most convincing way to verify directly the existence of astrophysical cold dark matter particles would be through their scattering on nuclei in low-background underground experiments [1]. Complementing this search for dark matter scattering in the laboratory via spin-independent (SI) and/or -dependent (SD) scattering, the next most direct way to search to confirm the nature of any such dark matter particles would be to observe products of their annihilations in an astrophysical context. Although less direct, observations of such annihilation products would provide valuable insight into the annihilation rates into important channels, which would provide more information on the dynamics of the dark matter particles, beyond their scattering cross sections. Observations of astrophysical annihilations of dark matter particles would be particularly interesting because cosmological annihilations earlier in the history of the Universe controlled the primordial relic abundance.

*John.Ellis@cern.ch
†olive@physics.umn.edu
‡savage@fysik.su.se
§vspanos@physics.upatras.gr

Several environments for annihilations of astrophysical dark matter particles are of interest, including the galactic halo [2], the galactic center [3], the Sun [4], the Earth [5], dwarf galaxies [6], and galaxy clusters [7]: our focus here is on the flux of neutralinos from dark matter annihilations inside the Sun. In this case, the dominant astrophysical uncertainties are the total line density of cold dark matter through which the Sun has passed throughout its history, and the mass fractions of different elements in the Sun, particularly for heavy nuclei (metals). In this paper we do not discuss the former, but we compare the predictions of models with different element compositions and discuss the importance of this model dependence for the observability of a signal.

There have been many studies of the prospective neutrino fluxes from solar dark matter annihilations in generic versions of the minimal supersymmetric extension of the standard model (MSSM), and also in specific versions such as the constrained MSSM (CMSSM) [8], in which the supersymmetry-breaking scalar and gaugino masses are each constrained to be universal at some input grand unified theory scale, and the lightest neutralino, $\chi$, is assumed to be the lightest supersymmetric particle (LSP) [9–11]. In this paper we study $\chi$ annihilations in the CMSSM, focusing, in particular, on the strips of parameter

space [10] where the relic $\chi$ density lies within the range of cold dark matter density indicated by WMAP [12] and other cosmological measurements. We also present more complete results for a few specific benchmark CMSSM scenarios [13], which are representative of the range of possibilities within the CMSSM.

The first step in calculating the flux of neutrinos from LSP annihilations inside the Sun is to calculate the LSP capture rate. This is controlled by the cross sections for LSP scattering on protons, which is mainly spin dependent in the CMSSM, and on heavier nuclei, which is mainly spin independent. Early work on capture often assumed that spin-dependent scattering would dominate, and neglected the spin-independent contribution from heavier nuclei, in particular. Secondly, one must check whether it is correct to assume that the LSP capture and annihilation processes in the Sun have reached equilibrium.

As we show later in this paper, neither of these assumptions is valid in general in the CMSSM: spin-independent scattering is also important, particularly at large values of $m_{1/2}$, and the annihilation rate is significantly smaller than the capture rate in large areas of the $(m_{1/2}, m_0)$ plane. Both these effects are particularly important at large $m_{1/2}$ along the coannihilation WMAP strip. We also discuss the differences in the annihilation rates calculated using different solar models.

The spin-dependent and -independent dark matter scattering rates both have significant uncertainties that affect the capture rate and hence also the annihilation rate [14–18]. The matrix element for spin-dependent scattering on a proton is related to the decomposition of the proton spin, in which the greatest uncertainty is the contribution of the strange quarks and antiquarks, $\Delta_s^{(p)}$. Inclusive deep-inelastic scattering experiments favor $\Delta_s^{(p)} = -0.09 \pm 0.03$ [19], whereas analyses of particle production in deep-inelastic scattering are quite compatible with $\Delta_s^{(p)} = 0$ [20]. In this paper, we compare the neutrino fluxes expected for $\Delta_s^{(p)} = 0$, $-0.06$, $-0.09$, and $-0.12$.

On the other hand, the matrix elements for spin-independent scattering on nuclei are related to the $\pi$-nucleon $\sigma$ term, $\Sigma_{\pi N}$, whose value is also quite uncertain. The central value in a theoretical analysis of low-energy $\pi$-nucleon scattering data is $\Sigma_{\pi N} = 64$ MeV [21], whereas $\Sigma_{\pi N} = 36$ MeV would correspond to the absence of a strange scalar density in the nucleon: $\langle N|\bar{s}s|N\rangle = 0$. We consider both these values, as well as the intermediate value $\Sigma_{\pi N} = 45$ MeV. Lattice calculations are now reaching the stage where they may also provide useful information on $\Sigma_{\pi N}$ [22], and a recent analysis would suggest a lower value $\Sigma_{\pi N} \lesssim 40$ [23]. For comparison, we also calculate the flux generated if spin-independent scattering is neglected altogether.

The layout of this paper is as follows. In Sec. II we discuss relevant aspects of the CMSSM, introducing general aspects of the $(m_{1/2}, m_0)$ planes for $\tan\beta = 10$ and 55

that we use as the basis for our subsequent calculations. In Sec. III we present various astrophysical considerations, including a comparison of the LSP capture and annihilation rates in the CMSSM, and a discussion of sensitivity to the solar model. In Sec. IV we discuss the sensitivities of the annihilation rates to uncertainties in the standard model, principally the hadronic matrix elements $\Delta_s^{(p)} = 0$ and $\Sigma_{\pi N}$ that control the spin-dependent and -independent scattering LSP-matter scattering cross sections, respectively, both of which are relevant, and the latter quite important. Then, in Sec. V we discuss the neutrino and neutrino-induced muon fluxes from LSP annihilations, first over the $(m_{1/2}, m_0)$ planes for $\tan\beta = 10$ and 55, subsequently along the WMAP strips in the coannihilation/rapid-annihilation and focus-point strips, and finally for four specific benchmark scenarios. We present results for three different neutrino thresholds: 1, 10, and 100 GeV. We find that restricted portions of the WMAP strips yield signals that may be detectable in the IceCube/DeepCore experiment [24,25]. In the coannihilation region, only models with small $m_{1/2}$ are detectable in IceCube/DeepCore. In the case of the focus-point region, a more extended part of the strip may be detectable in IceCube/DeepCore for $\tan\beta = 10$. For $\tan\beta = 55$, even in the focus-point region only models with small $m_{1/2}$ may be detectable in IceCube/DeepCore. These conclusions are not very sensitive to the uncertainties in the solar model and in $\Delta_s^{(p)} = 0$ that controls spin-dependent scattering, but the range of CMSSM parameter space that might be observable depends on the hadronic matrix element $\Sigma_{\pi N}$ controlling spin-independent scattering.

## II. CMSSM PARAMETER SPACE

We set the scene by first discussing the CMSSM parameter space that we explore. Points in the CMSSM are in principle characterized by four free parameters: the common gaugino mass, $m_{1/2}$, the common scalar mass, $m_0$, the common trilinear supersymmetry-breaking parameter, $A_0$, and the ratio of Higgs vacuum expectation values, $\tan\beta$. There is also an ambiguity in the sign of the Higgs mixing parameter, $\mu$: motivated by $g_\mu - 2$ and $b \to s\gamma$, we restrict our attention to positive $\mu$.[1] The three most relevant parameters for this analysis are $m_{1/2}$, $m_0$, and $\tan\beta$, and we present our results in the $(m_{1/2}, m_0)$ planes for the trilinear soft supersymmetry-breaking parameter $A_0 = 0$ and two discrete choices $\tan\beta = 10$, 55. The choice $\tan\beta = 10$ is close to the optimal value we find in a global likelihood analysis incorporating all the theoretical, phenomenological, experimental, and cosmological constraints on the CMSSM parameter space [26]. The choice $\tan\beta = 55$ is close to the maximum value for which we find consistent

---

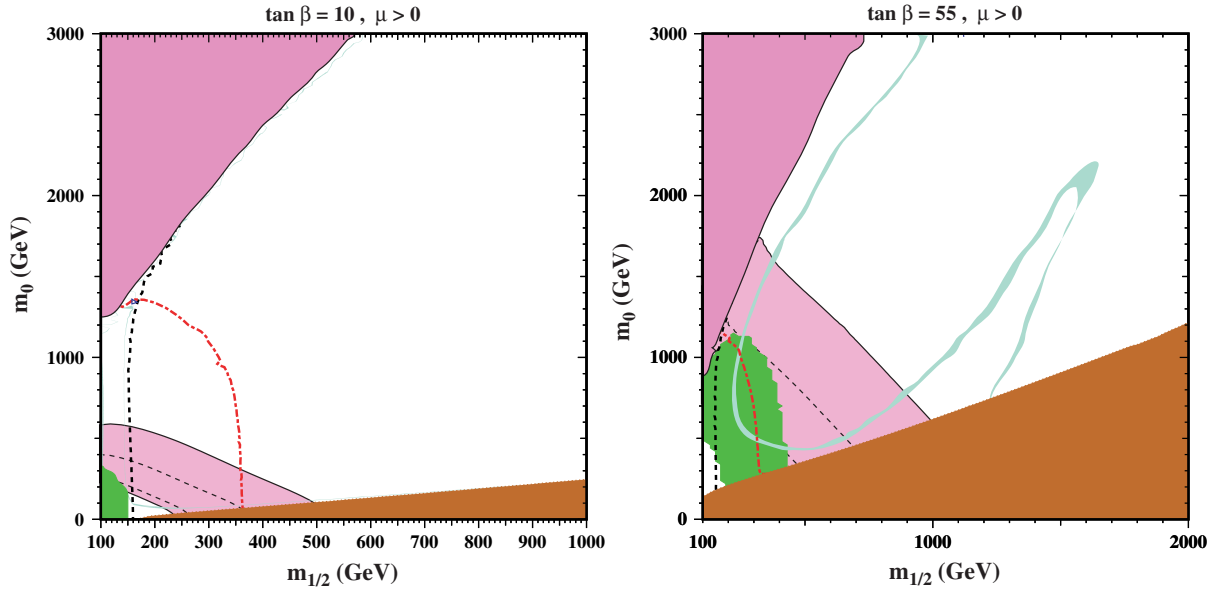[1]We neglect the possibility of significant *CP*-violating phases in the soft supersymmetry-breaking parameters.

FIG. 1 (color online). The $(m_{1/2}, m_0)$ planes for the CMSSM for $A_0 = 0$ and (left panel) $\tan\beta = 10$, (right panel) $\tan\beta = 55$, showing regions excluded because there is no consistent electroweak vacuum (dark pink shading), or because there is charged dark matter (brown shading), or because of a conflict with $b \to s\gamma$ measurements (green shading). Only regions to the right of the black dashed (red dash-dotted) line are consistent with the absence at LEP of charginos (Higgs boson). The turquoise strips are favored by the determination of the cold dark matter density by WMAP and other experiments [12], and the pink strips are favored by the BNL measurement of $g_\mu - 2$.

solutions of the CMSSM vacuum conditions, and represents the most distinct alternative from the favored case $\tan\beta = 10$.

In Fig. 1 and subsequent figures we display these $(m_{1/2}, m_0)$ planes with the following constraints implemented: regions lacking a consistent electroweak vacuum are found in the upper left corners of the figures (dark pink shading), regions with charged dark matter are found in the lower right corners (brown shading), the LEP bound on charginos [27] excludes the area to the left of the black dashed line and the LEP bound of 114.4 GeV on the Higgs mass [28] is shown by the (red) dash-dotted line (lighter Higgs masses occur to the left of this line). Here the code FEYNHIGGS [29] is used for the calculation of $m_h$. In addition we impose agreement with $b \to s\gamma$ measurements [30] which excludes the green shaded region at relatively low $m_{1/2}$. We also display the strips favored by the determination of the cold dark matter density by WMAP and other experiments [12] (turquoise shading). Also shown (shaded pink) is the band favored by the BNL measurement of $g_\mu - 2$ [31], using the latest estimate of the standard model contribution based on a compilation of $e^+e^-$ data including the most recent *BABAR* result [32], which leaves a discrepancy $\Delta(g_\mu - 2)/2 = (24.6 \pm 8.0) \times 10^{-10}$ [33] that could be explained by supersymmetry.[2]

In the case of $\tan\beta = 10$ (left panel of Fig. 1), there are two WMAP strips, one close to the boundary with charged dark matter where the neutralino coannihilates with the lighter stau and other sleptons, and the other close to the boundary of the region with an inconsistent electroweak vacuum, the focus-point region. In the case of $\tan\beta = 55$ (right panel of Fig. 1), the focus-point strip moves away from the electroweak vacuum boundary at large $m_0$ and small $m_{1/2}$, and connects with the coannihilation strip. The latter moves away from the charged dark matter region at small $m_0$ and large $m_{1/2}$, and bifurcates into strips on either side of a funnel where neutralinos annihilate rapidly via direct-channel $H$, $A$ poles.

In regions between the WMAP strips and the boundaries set by the absence of charged dark matter and the consistency of the electroweak vacuum, the calculated relic density falls below the WMAP range [12]. In these regions, for the purposes of our subsequent calculations we rescale the halo density by the ratio of the calculated cosmological density to the 2-$\sigma$ lower limit of the WMAP range. The same scaling is applied between the two sides of the funnel when $\tan\beta = 55$. Elsewhere, between the WMAP strips, the calculated density exceeds the WMAP range if one assumes conventional cosmology, but we nevertheless assume naively that the halo density is saturated by relic neutralinos. This would be possible, in principle, if some mechanism increased the entropy density between the epochs of dark matter freeze-out, when the temperature $T \sim m_\chi/20 \gtrsim 5$ GeV, and of cosmological nucleosythesis, when $T \lesssim 1$ MeV. We do not specifically advocate

_____

[2]The dashed lines include the 1-$\sigma$ range of $\Delta(g_\mu - 2)/2$, the solid lines the 2-$\sigma$ range.

such a scenario, but displaying complete $(m_{1/2}, m_0)$ planes enables us to put in context the results we present later for models along the WMAP strips. We also present more detailed results for representative benchmark points located on these strips.

## III. ASTROPHYSICAL CONSIDERATIONS

We review here the basic capture and annihilation processes and astrophysical considerations that affect these processes. The capture and annihilation of LSPs in the Sun depends both on the distribution of LSPs in the halo and on the abundances and distribution of elements within the Sun.

For the dark matter halo, we take a nonrotating isothermal sphere [34] with an rms speed of 270 km/$s$, a disk rotation speed of 220 km/$s$, and a local dark matter density of 0.3 GeV/cm$^3$, and we do not address other halo models in this paper. Our results would scale linearly with the local dark matter density as equilibrium between capture and annihilation is approached. For our fiducial solar model, we use the AGSS09 model of Serenelli *et al.* [35], which is based on the proto-solar isotopic abundances found in Ref. [36].

Gravitational capture of LSPs occurs when LSPs from the galaxy pass through the Sun, scatter off a nucleus, and lose enough energy that they can no longer escape from the Sun's gravitational potential. The capture rate per unit stellar mass via scattering off an isotope indexed by $i$ is given by [37,38]

$$\frac{dC_i}{dM}(v) = \frac{\rho_\chi \sigma_i}{m_\chi m_i} \epsilon_i \int d^3 u \frac{f(u)}{u} (u^2 + v^2) \mathcal{G}_i(u, v), \quad (1)$$

where $\rho_\chi$ is the LSP density, $m_\chi$ is the LSP mass, $m_i$ is the nuclear mass, $\sigma_i$ is the LSP-nuclear scattering cross section at zero momentum transfer, $\epsilon_i$ is the mass fraction of the isotope, $u$ is the LSP's velocity far away from the Sun, $v(r)$ is the velocity required for escape from the Sun, and

$$f(u) \equiv \frac{1}{4\pi} \int d\Omega f(\mathbf{u}) \quad (2)$$

is the angular-averaged LSP velocity distribution in the galactic neighborhood (in the Sun's frame, but outside the solar potential). Here,

$$\mathcal{G}_i(u, v) \equiv \frac{1}{E_{\max}} \int_{m_\chi u^2/2}^{E_{\max}} d(\Delta E) |F_i(\Delta E)|^2 \theta(\beta_- v^2 - u^2), \quad (3)$$

where

$$\beta_\pm \equiv \frac{4 m_\chi m_i}{(m_\chi \pm m_i)^2}, \quad (4)$$

$|F_i(\Delta E)|^2$ is a form factor (discussed below), $\Delta E$ is the energy imparted to a stationary nucleus in a collision with an LSP, and $E_{\max} = \frac{1}{2}\beta_+ m_\chi (u^2 + v^2)$ is the maximum

energy that can be imparted by an LSP with velocity $\sqrt{u^2 + v^2}$, where $\sqrt{u^2 + v^2}$ is the velocity of the LSP in the Sun. The quantity $\mathcal{G}_i(u, v)$ factors in two effects: (1) only a fraction of the scatters result in LSPs losing enough energy to become gravitationally bound, and (2) a form factor for finite momentum exchange can suppress higher-energy collisions. In the absence of a form factor ($|F_i|^2 = 1$), $\mathcal{G}_i(u, v)$ is just the fraction of scatters of an LSP at velocity $\sqrt{u^2 + v^2}$ on a stationary nucleus that yield a gravitationally bound LSP. The theta function $\theta(\beta_- v^2 - u^2)$ accounts for the fact that, for sufficiently large LSP velocities, scattering into bound orbits is not kinematically possible. The total capture rate is obtained by integrating Eq. (1) over the solar profile and summing over the isotopes present in the Sun.

The derivation of Eq. (1) is lengthy and the equations resulting from carrying out the integration are long and uniformative, so we do not include them here. Both the source of Eq. (1) and integrations are given by Gould in Refs. [37,38]. The capture rate is arrived at by different methods in those two references; our forms above closely match those of the latter, albeit with some small differences.[3] We refer the reader to those references for technical details and a more thorough discussion of the capture process. Here, we point out some of the features of Eqs. (1) and (3):

(i) The fraction of scatters that yield capture is largest for nuclei with masses nearest that of the LSP. Capture is suppressed for scattering off of light nuclei ($m_i \ll m_\chi$) as the LSP loses very little energy in these collisions and is more likely to maintain enough speed to escape the solar system and continue back out into the halo.

(ii) The fraction of scatters that yield capture is higher for scatters that occur deeper in the solar potential (larger $v$), i.e. when closer to the Sun's center.

(iii) Slow LSPs (small $u$) require less of an energy loss to become gravitationally bound and are more easily captured.

Scattering in the Sun is complicated by the fact that some LSP-nuclear interactions, particularly those involving heavy nuclei, are energetic enough that the finite size of the nucleus becomes important. In the zero-momentum-transfer limit, the LSP is expected to scatter coherently off the entire nucleus, which can effectively be treated as a point particle; an isotropic scattering cross section $\sigma_i$ is assumed in this case. When the inverse of the momentum $q$ exchanged in the scatter becomes comparable to or smaller than the size of the nucleus, the point-particle approxima-

---

[3]The quantity $\mathcal{G}(u, v)$ is equivalent to $\frac{1}{E_{\max}} G(u, v)$ in Ref. [38], while the LSP-nuclear scattering cross section $\sigma_i$ is equivalent to the quantity $\beta_+ m_\chi m_i \sigma_0 Q^2$. We also differ from Gould in that $f(u)$ is both the spatial and velocity phase space density in his derivations ($\int d^3 u f(u) = \rho_\chi / m_\chi$), as opposed to just the velocity phase space density here ($\int d^3 u f(u) = 1$).

tion is no longer valid and we must include a form factor: $\sigma_i \rightarrow \sigma_i |F(q^2)|^2$. We use simple exponential form factors,

$$|F(\Delta E)|^2 = e^{-\Delta E/E_0},$$

$$E_0 = \begin{cases} \frac{3\hbar^2}{2m_i r_i^2} & \text{(spin dependent)}, \\ \frac{5\hbar^2}{2m_i r_i^2} & \text{(spin independent)}, \end{cases} \quad (5)$$

where $m_i$ is the nuclear mass, $r_i$ is the effective nuclear radius, and $\Delta E = \frac{q^2}{2M}$ is the energy lost by the LSP in the collision. Capture rates with a form factor of this form can be found in the appendix of Ref. [37]. We differ here from Gould and other determinations of capture rates in that we use a different scale $E_0$ in the exponential for spin-dependent and spin-independent scattering.[4] For the latter case, this is a reasonable approximation to the more accurate Helm form factor for $\Delta E \lesssim 2E_0$ [39,40]. While the exponential form here becomes a poor approximation to the true form factor when $\Delta E \gg E_0$, the number of scattering events at such large energy losses are suppressed to the point that they make little contribution to the overall capture rate. The capture rate is thus sensitive mainly to the energy at which the form factor becomes important (i.e. $E_0$), not the shape of the form factor beyond this energy. The exponential form factor we use is therefore a reasonable approximation and use of e.g. the Helm form factor is not necessary for determining capture rates. This differs from direct detection searches, where the signal may be mainly high-energy scatters, for which a form factor that is accurate at large $\Delta E$ is necessary.

As gravitationally bound LSPs undergo additional scatters on subsequent passes through the Sun, they fall inward and approach thermal equilibrium at the center of the Sun. As the population of LSPs increases, the rate at which they annihilate with each other also increases; given sufficient time, the annihilation rate will come to equilibrium with the rate at which the LSPs are captured. The number $N$ of thermalized LSPs follows

$$\frac{dN}{dt} = C - C_E N - C_A N^2, \quad (6)$$

where $C$ is the capture rate, $C_E$ parametrizes the evaporation rate of the thermalized LSPs, and $C_A$ parametrizes the annihilation rate of the LSPs. Evaporation is only significant for LSPs lighter than $\sim 3$ GeV [41] and is neglected here, as we do not examine any models with such light LSPs. To a good approximation,

$$C_A = \langle \sigma_A v \rangle \left( \frac{3kT_c}{2Gm_\chi \rho_c} \right)^{-3/2}, \quad (7)$$

where $\langle \sigma_A v \rangle$ is the total LSP $s$-wave annihilation cross

section, $m_\chi$ is the LSP mass, and $T_c$ and $\rho_c$ are the temperature and density, respectively, at the center of the Sun. In the AGSS09 model, $T_c$ is $1.55 \times 10^7$ K and $\rho_c$ is 151 g/cm$^3$; these two quantities vary by negligible amounts for other solar models. Taking $C_E = 0$ and solving Eq. (6) yields an annihilation rate of

$$2\Gamma = C \tanh^2 \left( \frac{t_\odot}{\tau} \right), \quad (8)$$

where $t_\odot$ is the age of the Sun and $\tau = 1/\sqrt{CC_A}$. The factor of 2 in $2\Gamma$ is due to the loss of two LSPs in each annihilation event.

It is often assumed that, after the first scatter in which an LSP becomes gravitationally bound, it will quickly undergo additional scatters and come to thermal equilibrium in the center of the Sun. This assumption is not always valid: in some cases, further scatters may occur over time periods longer than the age of the Sun, in which case the LSPs have not yet reached thermal equilibrium, or the initial orbits may extend far enough out into the solar system that the LSPs are perturbed or gravitationally scattered by the planets, in which case they will never come to thermal equilibrium [42,43]. In both cases, the annihilation rate will be suppressed. However, for the CMSSM regions examined here, these effects are negligible and we ignore them.

### A. Comparison of capture and annihilation rates

As already mentioned, it might be thought that the LSP density within the Sun is in equilibrium, so that the annihilation rate is the same as the capture rate. However, as seen in Fig. 2, this is not in general true within the class of CMSSM scenarios discussed here.[5] In Fig. 2, we show contours of the ratio of the annihilation rate to the capture rate. Contours where this ratio exceeds 0.8 are in bold for clarity. In particular, for $\tan\beta = 10$, as seen in the left panel of Fig. 2, the LSP annihilation rate is in general much smaller than the capture rate, indicating that equilibrium is very poor approximation. The only regions in which equilibrium is approached are at very low $m_{1/2}$ where the LEP Higgs bound (red dash-dotted line) is violated, and close to the WMAP strip in the focus-point region, where annihilation exceeds 99% of the capture rate. In contrast, the annihilation rate falls to less than 1% of the capture rate along the coannihilation strip at large $m_{1/2}$. The loops centered at $m_{1/2} \approx 140$ GeV are due to a drop in the relic density due to rapid $s$-channel annihilation through the light Higgs boson. As a consequence, there are drops in both the capture and annihilation rates there. The kink and loop in the $(m_{1/2}, m_0)$ plane for $\tan\beta = 10$ (left panel of Fig. 2) centered at $m_{1/2} \sim 200$ GeV, where

---

[4]Note that Gould [37,38] defines the exponential scale in terms of the rms radius of the nucleus instead of the effective radius used here.

[5]In calculating the contours in this figure, we use the numerical AGSS09 [35] solar model and the default values of the hadronic matrix elements discussed below.
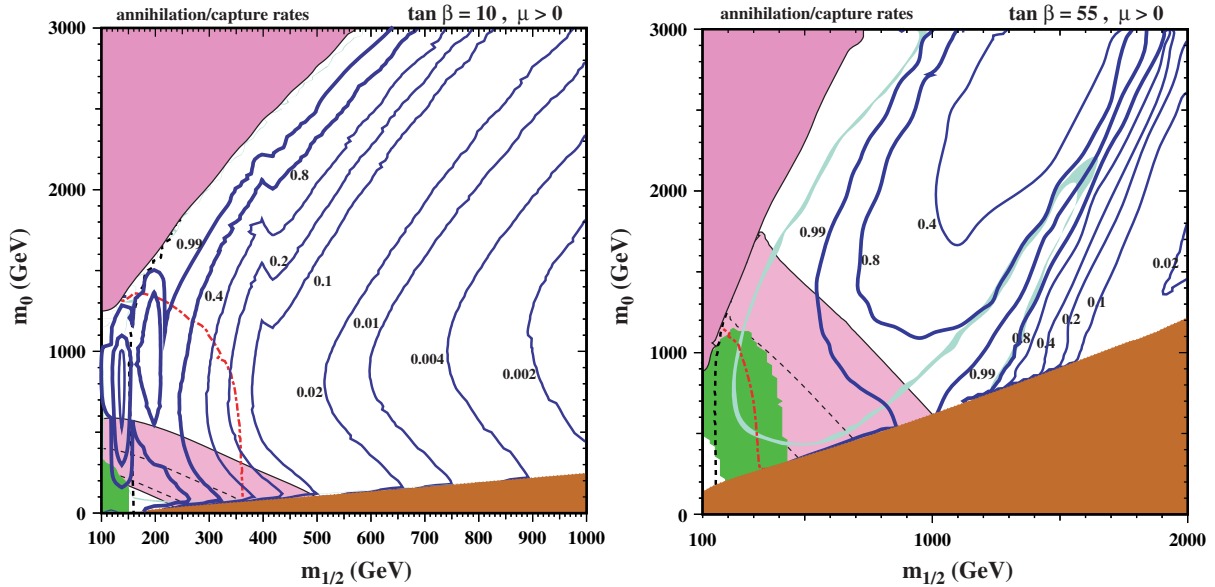
FIG. 2 (color online). The $(m_{1/2}, m_0)$ planes for the CMSSM for $A_0 = 0$ and (left panel) $\tan\beta = 10$, (right panel) $\tan\beta = 55$, showing contours of the ratio of solar dark matter annihilation and capture rates, as calculated using the AGSS09 model [35] and default values of the hadronic scattering matrix elements. Equilibrium corresponds to a ratio of unity, which is approached for small $m_{1/2}$ and large $m_0$. Also shown are the theoretical, phenomenological, experimental, and cosmological constraints described in the text.

the ratio of the annihilation and capture rates is relatively high, is due to the enhancement of annihilation just above the $W^+W^-$ threshold. The fluctuations in the contours of the ratio of the annihilation and capture rates for $m_{1/2} \sim 400$ GeV in the left panel of Fig. 2 reflect an increase in the annihilation rate above the $\bar{t}t$ threshold.

For $\tan\beta = 55$, as shown in the right panel of Fig. 2, there are larger regions where the annihilation rate exceeds 99% of the capture rate, extending to $m_{1/2} \sim 500$ GeV and more. In particular, equilibrium is approached in a significant fraction of the coannihilation strip, as well as along the focus-point strip, and also in the neighborhood of the rapid-annihilation funnel that extends to $m_{1/2} \sim 1500$ GeV, and beyond. This reflects the rapid increase in the annihilation cross section as one enters this funnel. We also note that the contours of the ratio of the annihilation and capture rates vary rapidly in the neighborhood of the rapid-annihilation funnel, particularly at larger $m_{1/2}$. As one approaches the funnel, the annihilation rate increases, thus increasing the ratio. At higher $m_{1/2}$, inside the funnel, the relic density is suppressed and the rates are scaled. At still larger $m_{1/2}$ the elastic cross section is suppressed and equilibrium is not recovered.

Being out of equilibrium has important consequences when we examine how variations in solar models and, later, scattering cross sections affect the annihilation rates and neutrino fluxes. In regions where capture and annihilation are in equilibrium ($t_\odot \gg \tau$), $2\Gamma \propto C$ so that, e.g. a 10% drop in the capture rate would lead to a $\sim 10\%$ drop in the annihilation rate. Since, for a given CMSSM model, the

neutrino flux is proportional to the annihilation rate, the neutrino flux would likewise decrease by $\sim 10\%$. However, when capture and annihilation are well out of equilibrium ($t_\odot \ll \tau$), $2\Gamma \propto C^2$. In this case, a 10% drop in the capture rate would lead to a $\sim 19\%$ drop in the annihilation rate and neutrino flux. Thus, the nonlinear dependence of Eq. (8) on the capture rate can amplify variations in the annihilation rate and hence the neutrino flux relative to the variations in the capture rate found in the various cases considered later in the paper.

### B. Dependence on the solar model

As discussed above, the rate at which the LSP is captured by the Sun involves determining both the rate at which galactic LSPs scatter in the Sun and the fraction of such scatters in which the LSP loses enough energy to become gravitationally bound to the Sun. The former depends on the LSP-nucleus scattering cross sections, while the latter depends on the mass of the nucleus off of which the LSP scatters; both factors may vary significantly among the different isotopes present in the Sun. The capture rate is thus sensitive to the abundances of elements in the Sun.

Serenelli *et al.* [35] have generated models of the Sun for several proto-solar isotopic abundances.[6] The models AGSS09 and AGSS09ph are based on the most recent estimates of these abundances [36]; the latter model differs

---

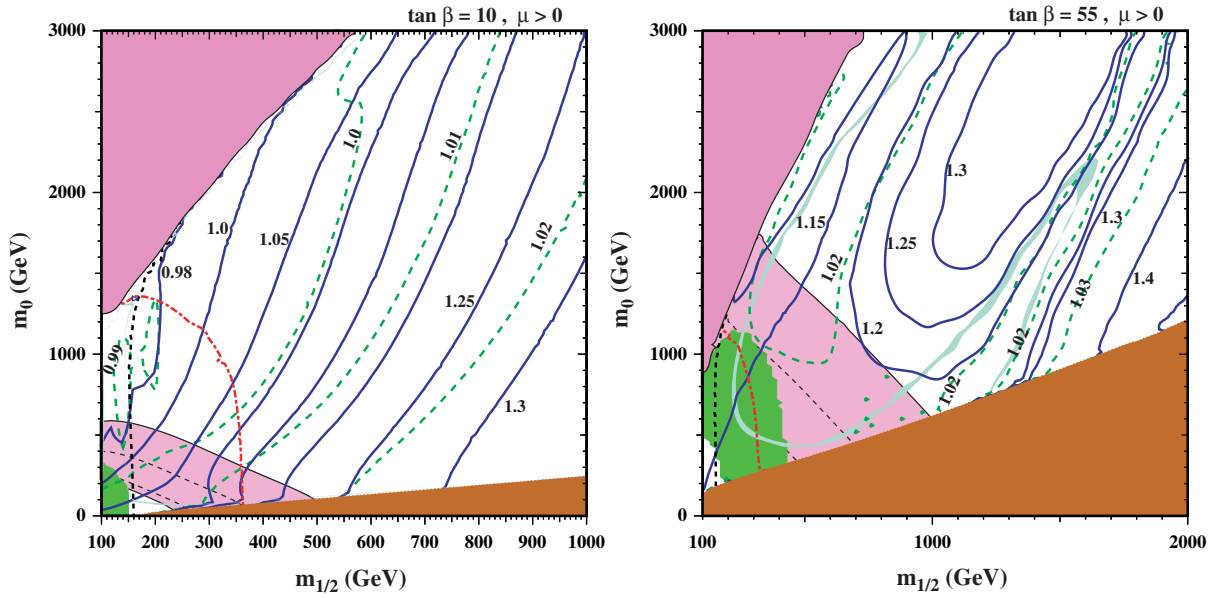[6]We include all 29 isotopes/elements maintained in these models when doing our calculations.

FIG. 3 (color online).　The $(m_{1/2}, m_0)$ planes for the CMSSM for $A_0 = 0$ and (left panel) $\tan\beta = 10$, (right panel) $\tan\beta = 55$ showing contours of the ratios of the solar dark matter annihilation rates calculated using the GS98 (solid lines) and AGSS09ph (dot-dashed lines) solar models to the annihilation rates found using the fiducial AGSS09 model [35]. Also shown are the theoretical, phenomenological, experimental, and cosmological constraints described in the text.

from the former in that photospheric measurements instead of meteoritic measurements are used to estimate abundances of refractory elements. Solar models based on recent abundance estimates are in conflict with helioseismological measurements of the Sun; Serenelli *et al.* provide an additional model (GS98), based on older abundance estimates [44], that is compatible with helioseismology. We show in Fig. 3 comparisons of the annihilation rates in the AGSS09ph and GS98 models with the fiducial case (AGSS09) in the planes for $\tan\beta = 10$ and 55.

The primary difference between the abundance sets and their corresponding solar models is an $\mathcal{O}(10)\%$ change in the metallicity in the Sun. While these metals represent less than 2% of the Sun's mass, we show later that capture via spin-independent interactions can be significantly enhanced by heavy nuclei due to a rapid increase in the scattering cross section. Moreover, the capture of heavy LSPs is favored kinematically by scattering on heavier elements. Because of these effects, these trace heavy elements can, in some cases, contribute a sizable portion of the total capture rate. We see in Fig. 3 that there is at most a 4% difference in the annihilation rates between the models based upon the two most recent abundance estimates (AGSS09 and AGSS09ph), so that the discrepancy between meteoritic and photospheric measurements is not a significant issue in estimating annihilation rates in CMSSM models. However, the model based on older abundance estimates that more closely matches helioseismology measurements (GS98) predicts annihilation rates as much as 40% higher. In both cases, the discrepancy grows larger as $m_{1/2}$ increases, since SI scattering, which occurs mainly off of the trace heavy elements that differ

among the models, becomes more important due to the aforementioned effects. In addition, part of the larger variation at higher $m_{1/2}$ can be attributed to nonequilibrium between capture and annihilation as discussed previously. For regions noted in Fig. 2 as being out of equilibrium, the variation in the capture rate for the different solar models is roughly half that of the variation in the annihilation rate. For regions in equilibrium, the variation in the capture rate is roughly the same as the variation in the annihilation rate.

It is unclear whether the discrepancies between the recent models and helioseismology are due to inaccuracies in the solar modeling or due to the most recent abundance estimates being incorrect; see [45] and references therein for further discussion of this issue. For this reason, uncertainties in the solar model still limit the precision to which annihilation rates (and, thus, neutrino fluxes) can be predicted for a given CMSSM model, but are not important for our conclusions.

### C. Approximating the solar potential

As shown by Gould [38], the calculation of the capture rate can be simplified if the solar potential is approximated by

$$\Phi(r) = \Phi_c - \frac{M(r)}{M_\odot}(\Phi_c - \Phi_s), \qquad (9)$$

where $M(r)$ is the mass of the Sun interior to a radial distance $r$, $\Phi_c$ and $\Phi_s$ are the gravitational potentials at the center and surface of the Sun, respectively, and $\Phi(r)$ is the potential at an arbitrary point in the Sun. This approximation yields an analytical form for the full capture rate,
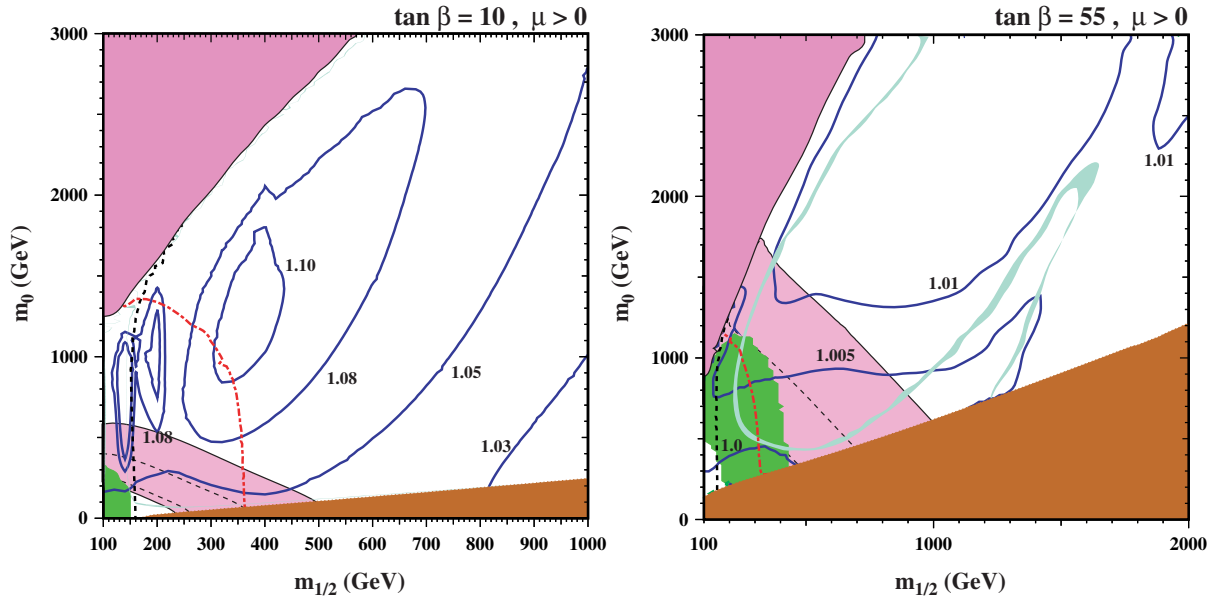
FIG. 4 (color online).   The $(m_{1/2}, m_0)$ planes for the CMSSM for $A_0 = 0$ and (left panel) $\tan\beta = 10$, (right panel) $\tan\beta = 55$ showing contours of the ratio of the dark matter annihilation rates calculated using a full numerical integration over the AGSS09 solar profile [35] and using an analytical approximation as proposed by Gould. Also shown are the theoretical, phenomenological, experimental, and cosmological constraints described in the text.

instead of requiring a numerical integration over the solar profile as necessary in the exact case. The analytical form is lengthy and can be found in Ref. [38].

The accuracy of the approximation is improved by choosing values for $\Phi_c$ and $\Phi_s$ such that Eq. (9) more closely follows the true potential profile (as determined in the numerical models) rather than using the actual central and surface potentials. We use $v_c = 1355$ km/s and $v_s = 818$ km/s for the central and surface escape velocities [where $\Phi(r) = -\frac{1}{2}v^2(r)$], which is obtained from a linear fit to the inner 90% (by mass) of the Sun in the AGSS09 model. The outer 10% is ignored in the fit as the potential can only be well approximated by a line for the inner $\sim$90%; inclusion of the outer layer makes the fit much poorer in the rest of the Sun. In addition, the dependence of Eq. (1) on the potential generally becomes most significant when capture is suppressed at the surface relative to the center; thus, a better fit to the inner regions of the Sun is preferred to a fit to the entire solar profile. For the parameters given above, Eq. (9) varies by less than 5% from the actual potential in the AGSS09 model for the inner 90% of the Sun. The fits to $v_c$ and $v_s$ for other solar models do not change significantly from the above values.

The Gould approximation requires the further assumption that the abundances of elements are uniform throughout the star. This is a reasonable approximation for elements heavier than oxygen, but is not a good approximation for lighter elements. Hydrogen and helium, in particular, are much more and less abundant, respectively, in the center of the Sun than elsewhere due to the hydrogen fusion occurring there. Carbon, nitrogen, and oxygen abun-

dances also vary throughout the star, under the influence of the CNO cycle. However, the combined CNO abundance is fairly uniform and, since these three elements have similar masses and cross sections, there is little loss in accuracy in taking a uniform abundance for them.

Looking at Fig. 4, we see that the numerical integration and the Gould approximation agree quite well in general, always within 11% in the $\tan\beta = 10$ plane, and better at high $m_{1/2}$ and in the focus-point region. For $\tan\beta = 55$, the accuracy is even better, with the approximation never varying more than 2% from the numerical result. The different levels of agreement between the numerical and analytical estimates have two sources: (1) varying levels of contribution between the spin-dependent and -independent scattering, and (2) amplification of differences when annihation and capture are out of equilibrium.

The capture rate itself is nearly uniformly overestimated by $\sim$8% for spin-dependent interactions and underestimated by $\sim$0.4% for spin-independent interactions when the Gould approximation is used. The approximation to the potential, Eq. (9), leads to a $\lesssim 1\%$ underestimate. The assumed uniformity of hydrogen throughout the Sun, however, gives a $\sim$8% overestimate of the capture via scattering off of hydrogen. As hydrogen accounts for over 99% of the captures via spin-dependent scatters,[7] but only a neg-

_____

[7]We have included spin-dependent scattering on all significant isotopes in the Sun (notably helium-3 and nitrogen-14), but find that elements other than hydrogen account for much less than 1% of the capture from this type of scattering in the models considered here.
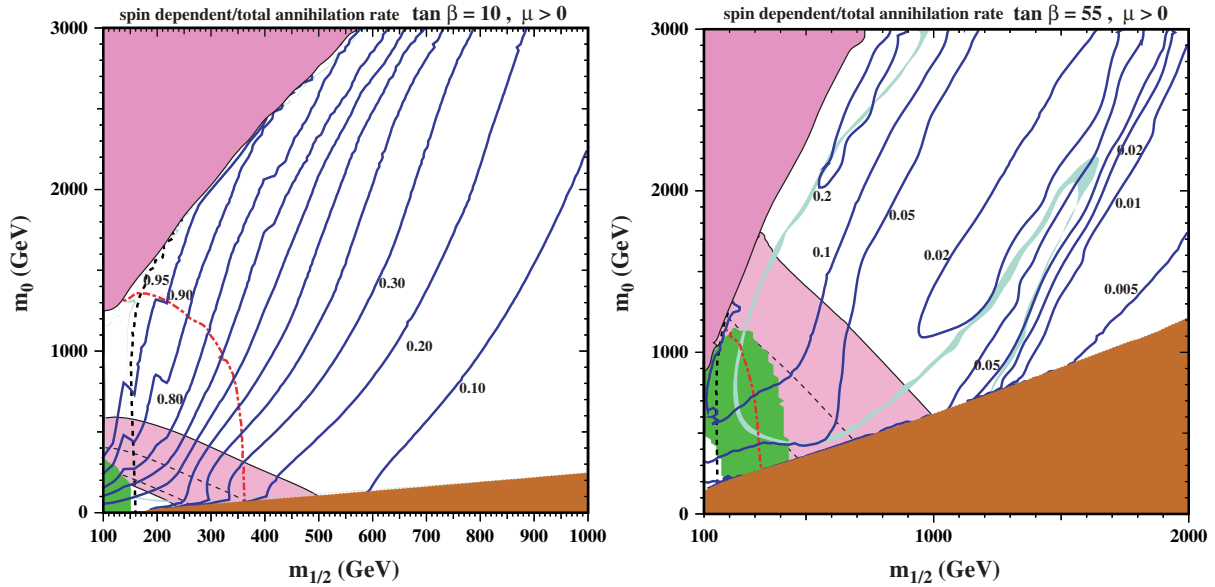
FIG. 5 (color online).   The $(m_{1/2}, m_0)$ planes for the CMSSM for $A_0 = 0$ and (left panel) $\tan\beta = 10$, (right panel) $\tan\beta = 55$ showing contours of the ratio of the solar dark matter annihilation rate calculated using only spin-dependent scattering to the total annihilation rate including also spin-independent scattering. Also shown are the theoretical, phenomenological, experimental, and cosmological constraints described in the text.

ligible portion of the capture via spin-independent scatters, spin-dependent capture is thus overestimated by $\sim 8\%$, while spin-independent capture remains underestimated by $\sim 0.4\%$. Note that helium is not the dominant nuclear target for spin-independent capture, so the poor assumption of uniform helium abundance has little bearing on the results. As seen in Fig. 5 and discussed in more detail below, spin-dependent scattering is a significant (and dominant for $\tan\beta = 10$) contribution to the total capture rate at small $m_{1/2}$, but is generally less significant at higher $m_{1/2}$, where spin-independent capture takes over. Thus, the Gould approximation becomes a better approximation at higher $m_{1/2}$.

The total capture rate varies by up to 6% with the approximation, with the largest difference occurring for $\tan\beta = 10$, where spin-dependent scattering is more significant. Again, nonequilibrium amplifies the variations, increasing 1%–6% variations in the capture rate to as much as 2%–11% variations in the annihilation rate. The largest variation in the annihilation rate, which occurs for $m_{1/2} \sim 300$–500 GeV in the $\tan\beta = 10$ plane (left panel of Fig. 4) occurs in the region where spin-dependent capture dominates and simultaneously annihilation is out of equilibrium. For higher values of $m_{1/2}$ in the $\tan\beta = 10$ plane, annihilation is still out of equilibrium, but spin-dependent scattering becomes less important. Though the nonequilibrium amplifies variations in the capture rate here, the capture rate for spin-independent scattering is much more accurate than the spin-dependent case, so the overall annihilation rate in the approximation becomes closer to the true value. For the $\tan\beta = 55$ case (right panel of

Fig. 4), spin-independent scattering dominates everywhere. Because the spin-independent capture rate is very accurately approximated, the approximation to the annihilation rate is quite accurate for $\tan\beta = 55$. The shapes of the contours in the right panel of Fig. 4 mainly result from the changing levels of equilibrium between annihilation and capture rather than from changes in the relative importance of spin-dependent and spin-independent scattering. In the focus-point and funnel regions, where annihilation and capture are in equilibrium, the variations in the annihilation rate reflect those of the capture rate ($\sim 0.5\%$–1%). In the area between the focus-point and funnel regions, where equilibrium is not maintained, the variation in the annihilation rate grows to roughly twice that of the capture rate ($\sim 1\%$–2%).

In principle, numerical integration over the true solar profile is certainly preferable to using the Gould approximation, because of its greater accuracy. However, there may be instances, such as computationally intensive scans over MSSM parameter space, where avoiding a numerical integration would be useful.[8] For example, using alternative form factors or LSP velocity distributions may require the integrals in Eq. (1) to be evaluated numerically, which could make determining the capture rate a computationally slow process where reducing the number of numerical integrations would be beneficial timewise. Also, we note that using this approximation introduces inaccuracies no worse than those due to choices in solar models and

---

[8]The same could be accomplished in some cases—but not all—by tabulating the integration, as done in DARKSUSY [46].

uncertainties in hadronic parameters, as discussed below. There is also room for improvement in this approximation as the chief source of its inaccuracy—the assumed uniformity of the hydrogen abundance—could be significantly alleviated by, e.g., breaking Eq. (9) into two parts, corresponding to the inner and outer portions of the Sun, and using more appropriate hydrogen abundances in each part.

## IV. STANDARD MODEL PARTICLE PHYSICS UNCERTAINTIES

We now turn to the uncertainties in the annihilation rates induced by the uncertainties in the hadronic matrix elements that enter into dark matter scattering rates, which are listed in Table I. They include those in the quark masses, expressed as $m_{d,c,b,t}$ and the ratios $m_u/m_d$ and $m_s/m_d$, those in the matrix elements $\langle N|\bar{q}q|N\rangle$—which are related to the change in the nucleon mass due to nonzero quark masses, denoted by $\sigma_0$, and therefore to the $\pi$-nucleon $\sigma$ term $\Sigma_{\pi N}$ as discussed later—and the axial-current matrix elements $\langle N|\bar{q}\gamma_\mu\gamma_5 q|N\rangle$, which are related to the quantities $\Delta_s^{(p)}$, $a_3^{(p)}$, and $a_8^{(p)}$, as also discussed later. The uncertainties in the elastic scattering cross section induced by the uncertainties in the quark masses, apart from the top quark, are negligible. However, cross-section uncertainties induced by the uncertainties in the matrix elements $\langle N|\bar{q}\gamma_\mu\gamma_5 q|N\rangle$ and $\langle N|\bar{q}q|N\rangle$ are important, as we discuss below. In particular, the uncertainties induced by our ignorance of $\Delta_s^{(p)}$ and particularly $\Sigma_{\pi N}$ should not be neglected.

As already mentioned, it might be thought that the dominant dark matter scattering process inside the Sun is spin-dependent scattering on the protons that comprise most of the solar mass. However, this is not necessarily the case in the CMSSM, as seen in Fig. 5 which shows the annihilation rate when only spin-dependent scattering is included, relative to the total annihilation rate when both

spin-dependent and -independent scattering is included. We see in the left panel for $\tan\beta = 10$ that, whereas spin-dependent scattering is indeed dominant at small $m_{1/2}$ and large $m_0$, this is a poor approximation already in the portion of the coannihilation strip that is favored by $g_\mu - 2$, and spin-independent scattering actually *dominates* at large $m_{1/2}$ along the coannihilation strip. For $\tan\beta = 55$ (right panel), spin-independent scattering dominates across the plane and significantly so in the coannihilation strip and in the rapid-annihilation funnel.[9] The increase in the relative importance of spin-independent scattering at large $m_{1/2}$ may be traced to the importance of the reduced neutralino mass $m_r$ in the kinematics of the scattering process. As the neutralino mass increases, the dependence on $m_r$ disfavors capture via scattering off light nuclei such as the proton that dominates spin-dependent scattering, and increases the relative importance of spin-independent scattering, which is dominated by scattering off more massive nuclei. Furthermore, because the spin-independent cross section increases with $\tan\beta$, its importance is amplified in the right panel for $\tan\beta = 55$. As in previous figures, we see in the right panel of Fig. 5 for $\tan\beta = 55$ that the contours of the ratio are relatively close together in the neighborhood of the rapid-annihilation funnel. In this region the annihilation rate varies rapidly and approaches equilibrium with the capture rate. Without spin-independent scattering, the capture rate there would be reduced, driving annihilation out of equilibrium and suppressing the annihilation rate and the resulting neutrino flux.

The results shown in Fig. 5 imply that one must discuss the uncertainties in both spin-dependent and -independent LSP scattering, as we discuss in more detail in the subsequent sections.

### A. Sensitivity to spin-dependent scattering

The SD part of the elastic $\chi$-nucleus cross section can be written as

$$\sigma_{\rm SD} = \frac{32}{\pi} G_F^2 m_r^2 \Lambda^2 J(J+1), \qquad (10)$$

where $m_r$ is the reduced neutralino mass, $J$ is the spin of the nucleus,

$$\Lambda \equiv \frac{1}{J}(a_p\langle S_p\rangle + a_n\langle S_n\rangle), \qquad (11)$$

$\langle S_p\rangle$ and $\langle S_p\rangle$ are the spin content of the proton and neutron groups, respectively [53], and

$$a_p = \sum_q \frac{\alpha_{2q}}{\sqrt{2}G_f}\Delta_q^{(p)}, \qquad a_n = \sum_i \frac{\alpha_{2q}}{\sqrt{2}G_f}\Delta_q^{(n)}. \qquad (12)$$

TABLE I. Strong-interaction parameters used to determine neutralino-nucleon scattering cross sections, with estimates of their experimental uncertainties. As discussed in the text, the most important uncertainties are those in $\sigma_0$, $\Sigma_{\pi N}$, and $\Delta_s^{(p)}$. We use as defaults for them the central values given in the table.

| | | |
|---|---|---|
| $m_u/m_d$ | $0.553 \pm 0.043$ | [47] |
| $m_d$ | $5 \pm 2$ MeV | [48] |
| $m_s/m_d$ | $18.9 \pm 0.8$ | [47] |
| $m_c$ | $1.27 \pm 0.09$ GeV | [48] |
| $m_b$ | $4.25 \pm 0.15$ GeV | [48] |
| $m_t$ | $173.1 \pm 1.3$ GeV | [49] |
| $\sigma_0$ | $36 \pm 7$ MeV | [50] |
| $\Sigma_{\pi N}$ | $64 \pm 8$ MeV | [16,21] |
| $a_3^{(p)}$ | $1.2694 \pm 0.0028$ | [48] |
| $a_8^{(p)}$ | $0.585 \pm 0.025$ | [51,52] |
| $\Delta_s^{(p)}$ | $-0.09 \pm 0.03$ | [19] |

---

[9]In calculating the contours in this figure, we use the default values of $\Delta_s^{(p)}$ and $\Sigma_{\pi N}$ discussed below.
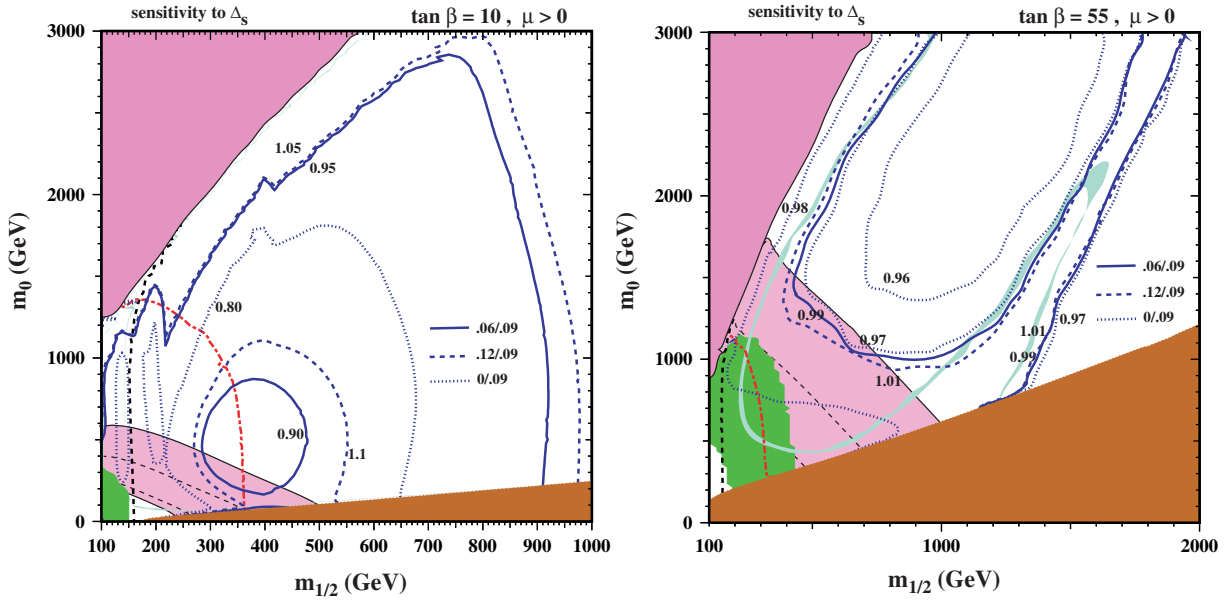
FIG. 6 (color online). The $(m_{1/2}, m_0)$ planes for the CMSSM for $A_0 = 0$ and (left panel) $\tan\beta = 10$, (right panel) $\tan\beta = 55$ showing contours of the ratios of the annihilation rates calculated assuming $\Delta_s^{(p)} = 0.00$ (dotted lines), $-0.06$ (solid lines), and $-0.12$ (dashed lines) to calculations with the default value $\Delta_s^{(p)} = -0.09$. Also shown are the theoretical, phenomenological, experimental, and cosmological constraints described in the text.

The factors $\Delta_q^{(N)}$ parametrize the quark spin content of the nucleon and are significant only for the light ($u$, $d$, $s$) quarks. A combination of experimental and theoretical results tightly constrains the linear combinations [48]

$$a_3^{(p)} \equiv \Delta_u^{(p)} - \Delta_d^{(p)} = 1.2694 \pm 0.0028 \qquad (13)$$

and [51,52]

$$a_8^{(p)} \equiv \Delta_u^{(p)} + \Delta_d^{(p)} - 2\Delta_s^{(p)} = 0.585 \pm 0.025. \qquad (14)$$

However, determination of the individual $\Delta_q^{(N)}$ requires a third piece of information, usually taken to be the strange spin contribution $\Delta_s^{(p)}$, as extracted from inclusive deep-inelastic lepton-nucleon scattering. Using, e.g., the recent COMPASS result [19], one has

$$\Delta_s^{(p)} = -0.09 \pm 0.01(\text{stat}) \pm 0.02(\text{syst}) \approx -0.09 \pm 0.03, \qquad (15)$$

where, conservatively, we have combined linearly the statistical and systematic uncertainties. Using this range for $\Delta_s^{(p)}$, we may express $\Delta_{u,d}^{(N)}$ as follows in terms of known quantities:

$$\Delta_u^{(p)} = \tfrac{1}{2}(a_8^{(p)} + a_3^{(p)}) + \Delta_s^{(p)} = 0.84 \pm 0.03, \qquad (16)$$

$$\Delta_d^{(p)} = \tfrac{1}{2}(a_8^{(p)} - a_3^{(p)}) + \Delta_s^{(p)} = -0.43 \pm 0.03. \qquad (17)$$

The above two uncertainties are almost completely corre-

lated with that of $\Delta_s^{(p)}$, however, and the uncertainties in $a_3^{(p)}$ and $a_8^{(p)}$ are negligible by comparison. We use the central value in Eq. (15) as our default, namely $\Delta_s^{(p)} = -0.09$.[10]

For comparison, in Fig. 6 we compare the annihilation rates calculated using this default value and with $\Delta_s^{(p)} = -0.12$ and $-0.06$. We recall, however, that analyses of $\pi$ and $K$ meson production in deep-inelastic scattering have been interpreted as suggesting that $\Delta_s^{(p)}$ may be compatible with zero [20]. Accordingly, we also present in Fig. 6 results for this extreme value of $\Delta_s^{(p)}$.

In general, the spin-dependent scattering rate increases and decreases with $\Delta_s^{(p)}$, and the effect is quite symmetric for $\Delta_s^{(p)} \in (-0.12, -0.06)$. However, the effect is quite small for $\Delta_s^{(p)}$ within this range, differing from the rate calculated with our default assumption $\Delta_s^{(p)} = -0.09$ by at most $\sim 10\%$ for small $m_{1/2}$ when $\tan\beta = 10$ (left panel of Fig. 6) and considerably less for $\tan\beta = 55$ (right panel of Fig. 6).[11] However, the reduction may be considerably larger if $\Delta_s^{(p)} = 0$, potentially exceeding 20% at small $m_{1/2}$ when $\tan\beta = 10$.

---

[10]We recall that the proton and neutron scalar matrix elements are related by an interchange of $\Delta_u$ and $\Delta_d$, i.e., $\Delta_u^{(n)} = \Delta_d^{(p)}$, $\Delta_d^{(n)} = \Delta_u^{(p)}$ and $\Delta_s^{(n)} = \Delta_s^{(p)}$.

[11]The contours near the rapid-annihilation funnel again reflect the equilibrium/nonequilibrium effects on the annihilation rate discussed earlier.

### B. Sensitivity to spin-independent scattering

The SI part of the cross section for scattering on a nucleus $(Z, A)$ can be written as

$$\sigma_{SI} = \frac{4m_r^2}{\pi}[Zf_p + (A - Z)f_n]^2, \qquad (18)$$

where $m_r$ is the $\chi$-nuclear reduced mass and

$$\frac{f_N}{m_N} = \sum_{q=u,d,s} f_{T_q}^{(N)}\frac{\alpha_{3q}}{m_q} + \frac{2}{27}f_{TG}^{(N)}\sum_{q=c,b,t}\frac{\alpha_{3q}}{m_q} \qquad (19)$$

for $N = p$ or $n$. The parameters $f_{T_q}^{(N)}$ are defined by

$$m_N f_{T_q}^{(N)} \equiv \langle N|m_q\bar{q}q|N\rangle \equiv m_q B_q^{(N)}, \qquad (20)$$

where [54,55]

$$f_{TG}^{(N)} = 1 - \sum_{q=u,d,s} f_{T_q}^{(N)}. \qquad (21)$$

We take the ratios of the light quark masses from [47]:

$$\frac{m_u}{m_d} = 0.553 \pm 0.043, \qquad \frac{m_s}{m_d} = 18.9 \pm 0.8, \qquad (22)$$

and the other quark masses are taken from [48], except for the top mass, which is taken from the combined CDF and D0 result [49]. These masses, as well as other experimental quantities that will arise in the calculation of the hadronic matrix elements, appear in Table I.

Following [56], we introduce the quantity:

$$z \equiv \frac{B_u^{(p)} - B_s^{(p)}}{B_d^{(p)} - B_s^{(p)}} = 1.49, \qquad (23)$$

which has an experimental error that is negligible compared with others discussed below, and the strange scalar density

$$y \equiv \frac{2B_s^{(N)}}{B_u^{(N)} + B_d^{(N)}}. \qquad (24)$$

In terms of these quantities, one may write

$$\frac{B_d^{(p)}}{B_u^{(p)}} = \frac{2 + ((z - 1) \times y)}{2 \times z - ((z - 1) \times y)}. \qquad (25)$$

Proton and neutron scalar matrix elements are related by an interchange of $B_u$ and $B_d$, i.e.,

$$B_u^{(n)} = B_d^{(p)}, \qquad B_d^{(n)} = B_u^{(p)}, \quad \text{and} \quad B_s^{(n)} = B_s^{(p)}. \qquad (26)$$

The $\pi$-nucleon sigma term, $\Sigma_{\pi N}$, may be written as

$$\Sigma_{\pi N} \equiv \tfrac{1}{2}(m_u + m_d) \times (B_u^{(N)} + B_d^{(N)}), \qquad (27)$$

and the coefficients $f_{T_q}$ may be written in the forms:

$$f_{T_u} = \frac{m_u B_u}{m_N} = \frac{2\Sigma_{\pi N}}{m_N(1 + \frac{m_d}{m_u})(1 + \frac{B_d}{B_u})}, \qquad (28)$$

$$f_{T_d} = \frac{m_d B_d}{m_N} = \frac{2\Sigma_{\pi N}}{m_N(1 + \frac{m_u}{m_d})(1 + \frac{B_u}{B_d})}, \qquad (29)$$
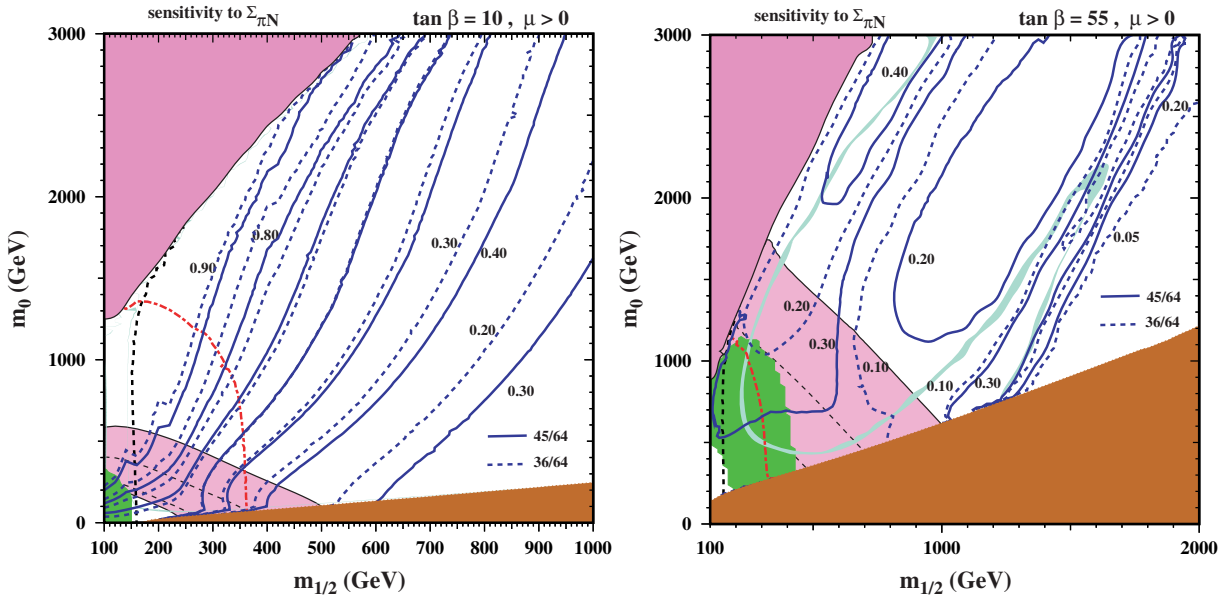


FIG. 7 (color online). The $(m_{1/2}, m_0)$ planes for the CMSSM for $A_0 = 0$ and (left panel) $\tan\beta = 10$, (right panel) $\tan\beta = 55$ showing contours of the ratios of the solar dark matter annihilation rates calculated using $\Sigma_{\pi N} = 36$ MeV (dashed lines) and 45 MeV (solid lines) to calculations with the default value $\Sigma_{\pi N} = 64$ MeV. Also shown are the theoretical, phenomenological, experimental, and cosmological constraints described in the text.

$$f_{T_s} = \frac{m_s B_s}{m_N} = \frac{(\frac{m_s}{m_d})\Sigma_{\pi N} y}{m_N(1 + \frac{m_u}{m_d})}, \tag{30}$$

where we have dropped the $(N)$ superscript from $f_{T_q}$ and $B_q$.

The effects of the uncertainties in the $f_{T_q}$ were considered in [57], and we were motivated to study [16] variations in the value of $y$ by reevaluations of the $\pi$-nucleon sigma term $\Sigma_{\pi N}$, which is related to the strange scalar density in the nucleon by

$$y = 1 - \sigma_0 / \Sigma_{\pi N}. \tag{31}$$

The value for $\sigma_0$ given in Table I is estimated on the basis of octet baryon mass differences to be $\sigma_0 = 36 \pm 7$ MeV [50,58–60]. Based on recent determinations of $\Sigma_{\pi N}$ at the Cheng-Dashen point [21], one finds

$$\Sigma_{\pi N} = (64 \pm 8) \text{ MeV}. \tag{32}$$

We use the central value in Eq. (32) as our default, namely $\Sigma_{\pi N} = 64$ MeV.

In Fig. 7, we compare the annihilation rates calculated with this default value and with $\Sigma_{\pi N} = 45$ or 36 MeV, the latter corresponding via Eq. (31) to the central value for $\sigma_0$, i.e., $y = 0$. As could be expected from the previous analysis demonstrating the importance of spin-independent scattering at large $m_{1/2}$, we see that the annihilation rate decreases very substantially if $\Sigma_{\pi N}$ is decreased to 45 or 36 MeV.[12] As in the case of direct dark matter detection via spin-independent scattering, it is also very important for the interpretation of indirect dark matter searches via neutrinos from dark matter annihilation inside the Sun to pin down the magnitude of $\Sigma_{\pi N}$.

## V. NEUTRINO AND MUON FLUXES

Neutrino detectors such as IceCube/DeepCore [24,25] aim to detect the capture of LSPs in the Sun using neutrinos produced in the LSP annihilations. The primary experimental signature is the passage of neutrino-induced muons through the detector. Here, we examine the flux of neutrinos and neutrino-induced muons in the $\tan\beta = 10$ and 55 planes, as well as along the WMAP-preferred focus-point, coannihilation, and funnel-region strips (the last for $\tan\beta = 55$ only). We also study the neutrino and flux spectra for several benchmark scenarios given in Table II.

Determining the neutrino spectrum in a detector involves two steps: (1) the production of neutrinos from LSP annihilations, and (2) propagation of the neutrinos from the interior of the Sun to the detector. Low-energy neutralinos do not generally annihilate directly into neutrinos; instead, neutrinos are produced in decays/showers

of the primary annihilation particles such as $W$ bosons, top quarks, or tau leptons (e.g. $\chi\chi \to \tau\bar{\tau}$, with $\tau \to \mu\bar{\nu}_\mu\nu_\tau$). Determination of the neutrino spectra in such showers is complicated by the fact that they occur in the dense center of the Sun, so that the primary particles may lose energy before decaying [61–64].

Once neutrinos are produced, they must travel through the Sun, where they may undergo charged-current or neutral-current interactions that absorb the neutrinos or reduce the neutrino energies, respectively. The Sun is mainly transparent to neutrinos well below $\sim 100$ GeV, but becomes opaque when the energies reach $\sim 200$–300 GeV; thus, high-energy neutrinos are heavily suppressed. Oscillations between neutrino species between the Sun and Earth must also be taken into account [65].

We use the neutrino and neutrino-induced muon spectra determined by WIMPSIM [66] (and used within DARKSUSY [46]), which simulated both of the steps described above to generate spectra for several LSP annihilation channels. Neutrino production and propagation has also been simulated in Ref. [67].[13]

For our neutrino spectrum results here, we neglect Higgs annihilation channels and include only annihilations into quarks, leptons, $W$ and $Z$ bosons. The Higgs channels account for less than 3% of the annihilations in all the $\tan\beta = 10$ region we have considered and, apart from a small region at $m_{1/2} > 1900$ GeV just above the charged dark matter constraint (brown region in the planar figures), Higgs channels account for less than 10% of the annihilations in the $\tan\beta = 55$ plane. In most cases, and all of the WMAP strips, the Higgs channels account for $\sim 1\%$ or less of the annihilations. The error introduced by neglecting the Higgs channels is thus far smaller than variations induced by the choice of solar model or uncertainties in the hadronic parameters discussed previously.

The muon energy detection threshold $E_{\text{th}}$ is an important consideration in determining the sensitivity of neutrino detectors to annihilations in the Sun. Increasing the exposure area of a detector often requires a sacrifice in the energy threshold. Since high-energy neutrinos from the Sun (and thus muons) are suppressed, high thresholds may inhibit detectors from observing this type of signal. The full IceCube detector will have a fairly large effective area, but gradually loses sensitivity to muons below energies $\sim 100$ GeV due to the large spacing between strings [24]. A smaller portion of the detector, referred to as DeepCore, will be instrumented more densely and with higher efficiency phototubes to allow for detection of lower-energy muons; DeepCore can potentially detect muons down to energies of 10 GeV or lower [25]. The effective neutrino detection area of the combined IceCube/

---

[12]The contours near the rapid-annihilation funnel again reflect the nonequilibrium effects on the annihilation rate discussed earlier.

[13]During the preparation of this paper, an error was discovered in the antineutrino fluxes of Ref. [67] that prevented us from making full use of their results at this time.

TABLE II. CMSSM parameters and results for benchmark models C, E, L, and M of [13]. $E_{th}$ is the neutrino/muon energy threshold. Rates and fluxes are determined using the AGSS09 solar model and the central values found in Table I for the hadronic parameters.

| Model | C | E | L | M |
|---|---|---|---|---|
| $m_{1/2}$ (GeV) | 400 | 300 | 460 | 1075 |
| $m_0$ (GeV) | 96 | 2003 | 312 | 1045 |
| $\tan\beta$ | 10 | 10 | 50 | 55 |
| $A_0$ | 0 | 0 | 0 | 0 |
| $\text{sign}(\mu)$ | + | + | + | + |
| $m_\chi$ (GeV) | 165 | 117 | 193 | 474 |
| Capture rate (/s) | $2.58 \times 10^{20}$ | $4.97 \times 10^{22}$ | $1.05 \times 10^{21}$ | $9.79 \times 10^{18}$ |
| Annihilation rate [$2\Gamma$] (/s) | $8.72 \times 10^{19}$ | $4.97 \times 10^{22}$ | $1.05 \times 10^{21}$ | $8.75 \times 10^{18}$ |
| Neutrino flux (/km$^2$/yr) | | | | |
| $\quad E_{th} = 1$ GeV | $3.27 \times 10^9$ | $9.19 \times 10^{11}$ | $3.33 \times 10^{10}$ | $2.16 \times 10^8$ |
| $\quad E_{th} = 10$ GeV | $2.60 \times 10^9$ | $7.03 \times 10^{11}$ | $2.43 \times 10^{10}$ | $1.47 \times 10^8$ |
| $\quad E_{th} = 100$ GeV | $2.86 \times 10^8$ | $8.80 \times 10^9$ | $3.26 \times 10^9$ | $3.35 \times 10^7$ |
| Muon flux (/km$^2$/yr) | | | | |
| $\quad E_{th} = 1$ GeV | 5.98 | 1210 | 61.8 | 0.830 |
| $\quad E_{th} = 10$ GeV | 4.71 | 898 | 49.7 | 0.734 |
| $\quad E_{th} = 100$ GeV | 0.129 | 0.243 | 2.70 | 0.222 |

DeepCore detector falls from $\sim 1$ m$^2$ at 1 TeV, to $\sim 10^{-2}$ m$^2$ at 100 GeV, to $\sim 10^{-4}$ m$^2$ at 10 GeV, with IceCube providing nearly all of the effective area above 100 GeV and DeepCore providing nearly all of it below 30 GeV.

The ability of IceCube/DeepCore to observe a signal above background for a particular CMSSM model depends on the neutrino spectrum, angular spread of the induced muons, backgrounds, and detector geometry [68,69]. The predominant backgrounds are muons and muon neutrinos generated from cosmic ray interactions in the atmosphere; cosmic ray interactions in the Sun may also contribute to the background [70]. When looking for a signal from a point source such as the Sun, the diffuse background is reduced by making angular cuts on the observed muon event directions. A signal analysis is complicated by the fact that the angular spread of solar neutrino-induced muons is dependent on neutrino energies, so that optimal data cuts are dependent on the expected neutrino spectrum for a particular CMSSM model. In addition, the angular and energy resolutions and the effective area for muon events, particularly at low energies, are dependent on the detector geometry. Such a careful analysis is beyond the scope of this paper.

Still, we can roughly approximate the IceCube/DeepCore sensitivity to estimate the detectability of various CMSSM models. IceCube/DeepCore has generated a conservative sensitivity limit for muons above 1 GeV in their detector assuming a particular hard annihilation spectrum [69] ($\tau\bar{\tau}$ for $m_\chi < 80$ GeV, $W^+W^-$ at higher masses). The fraction of annihilations into channels that yield hard spectra ($\chi\chi \rightarrow ZZ$, $W^+W^-$, $t\bar{t}$ or $\tau\bar{\tau}$) is never

trivial in the CMSSM models we consider in this paper. In the $\tan\beta = 10$ case, 70%–99% of the annihilations are into one of these hard channels, while in the $\tan\beta = 55$ case 20%–50% of the annihilations are into one of these channels. The fractions of annihilations into soft spectra channels (e.g. $\chi\chi \rightarrow b\bar{b}$) are 1%–30% and 50%–80% for the $\tan\beta = 10$ and 55 cases, respectively. Thus, in all cases, the spectrum produced in a CMSSM model will contain a significant hard component. Since these CMSSM neutrino spectra differ from the spectra used by IceCube/DeepCore to generate their muon flux limits, the IceCube/DeepCore muon flux limits cannot be directly applied to particular CMSSM models. However, the significant hard component of the CMSSM spectrum should be similar enough to the hard spectrum channels analyzed by IceCube/DeepCore that the sensitivity limits are within a factor of 2 ($\tan\beta = 10$) or 2–5 ($\tan\beta = 55$) of the sensitivity that would be obtained had the actual neutrino spectra been used in the analysis. Hence, in the $\tan\beta = 55$ case, the limits obtainable are expected to be somewhat weaker than in the $\tan\beta = 10$ case, due to the lower fraction of annihilations into hard channels.

The IceCube/DeepCore projected sensitivity is shown in Figs. 9–11, normalized to the total expected muon flux above 1 GeV (though the experiment is only weakly sensitive to muons at such low energies).[14] We note that the IceCube/DeepCore collaboration characterizes this as a "conservative" limit, and that the sensitivity could be

---

[14]If the actual spectrum were to be entirely soft, the IceCube/DeepCore muon flux sensitivity would be weakened by an order of magnitude or more.

further improved in several possible ways. For example, (1) data are generally used only from periods when the Sun is below the horizon, as this reduces the cosmic-ray backgrounds. However, it may be possible to use the surrounding IceCube portion of the detector to veto cosmic-ray-induced events in the DeepCore portion of the detector, allowing data from daylight hours to be included in the analysis and hence potentially doubling the exposure at low energies. In addition, (2) even a few more strings placed in the DeepCore region (a very interesting possibility in light of our analysis) would significantly improve sensitivity to low-energy muons. For these reasons, the IceCube/DeepCore muon flux sensitivity limits should be taken only as an order of magnitude estimate when assessing the detectability of the CMSSM models below.

### A. Fluxes in $(m_{1/2}, m_0)$ planes

We present in Fig. 8 contours of the neutrino-induced muon fluxes in the $(m_{1/2}, m_0)$ planes for $\tan\beta = 10$ (left panels) and $\tan\beta = 55$ (right panels), for three values of the detector threshold: 1 GeV (top row), 10 GeV (middle row), and 100 GeV (bottom row). The other phenomenological, experimental, and cosmological constraints are as in Fig. 2. As the aforementioned sensitivity limits cannot easily be applied to these figures, we can expect, to a very rough approximation, IceCube to detect muon fluxes on the order of 10 or $10^2/\text{km}^2/\text{yr}$ above $\sim 100$ GeV and DeepCore to detect muon fluxes on the order of $10^2$ or $10^3/\text{km}^2/\text{yr}$ above $\sim 10$ GeV.

For $\tan\beta = 10$, the muon flux attains its maximum value close to the focus-point region. The picture does not change much when the detector threshold increases from 1 to 10 GeV, but for threshold 100 GeV the contours show lower muon fluxes. IceCube/DeepCore is in this case expected to probe all the focus-point region and much of the bulk region. Note that although the highest flux contour we display is $500/\text{km}^2/\text{yr}$, the flux continues to increase as one approaches the region where radiative electroweak symmetry breaking no longer is viable. The focus-point strip is very close to this boundary and indeed the flux does exceed $10^3/\text{km}^2/\text{yr}$ when the relic density is in the WMAP range. This will be seen more clearly when we discuss the WMAP strips in the next section. The focus-point region produces the largest fluxes observable by IceCube alone (high threshold, bottom left panel of Fig. 8); these high-energy muon fluxes may even be detectable without including the sensitivity to lower-energy muons that DeepCore provides. The same holds for $\tan\beta = 55$: the neutrino-induced muon flux is again largest in the focus-point region, close to the region theoretically excluded due to the absence of electroweak symmetry breaking. However, the fluxes are likely too low to be observed by IceCube/DeepCore, except for the lowest values of $m_{1/2}$ along this strip. The cosmologically favored region around the rapid-annihilation funnel yields much smaller values

for the muon fluxes, below the expected experimental sensitivities.

### B. Fluxes along WMAP strips

In Fig. 9, we plot the neutrino-induced muon fluxes in the cosmologically favored regions of the CMSSM that are also compatible with the rest of the phenomenological and experimental constraints, namely, the regions that we call WMAP strips. These strips are determined by fixing the value of $m_0$ so that at each value of $m_{1/2}$ (or equivalently $m_\chi \approx 0.43 m_{1/2}$) the relic density is within the $2\sigma$ WMAP range [12]. We pick again the same representative values of $\tan\beta = 10$ (left panel) and 55 (right panel). For $\tan\beta = 10$, there are two such strips corresponding to either the coannihilation or focus-point regions. For $\tan\beta = 55$, the coannihilation strip runs into the funnel region at large $m_\chi$. At very large $m_\chi$, we have sampled both sides of the funnel resulting in a "doubling back" of the curves we display.

A conservative IceCube/DeepCore sensitivity limit for muon fluxes above 1 GeV is also shown in the figure. As discussed previously, this sensitivity cannot be directly applied to the CMSSM fluxes shown as the spectra differ. However, the limit should be within a factor of 2 or so of the muon fluxes necessary to detect these CMSSM models (recall that, if additional strings are added to DeepCore and/or data can be used from periods when the Sun is above the horizon, the IceCube/DeepCore sensitivity could be as much as an order of magnitude better than shown).

As observed in Fig. 8, the muon flux is largest in the focus-point region for both values of $\tan\beta$. In Fig. 9 (left panel) we plot the values for the muon fluxes along the coannihilation strip (solid curves) and the focus-point strip (dashed curves) for $\tan\beta = 10$. The blue, red, and green curves correspond to threshold energies 1, 10, and 100 GeV. In the focus-point region, the muon flux is $\sim 10^2$–$10^3/\text{km}^2/\text{yr}$, making detection in IceCube/DeepCore a likely possibility, particularly for lighter LSPs (smaller $m_{1/2}$). For $\tan\beta = 55$ (right panel), the solid curves represent both the coannihilation and funnel strips. The double covering of $m_\chi \sim 550$–750 GeV is due to the shape of the WMAP strip in the funnel region, as noted above. As already observed, the values of the muon fluxes are similar in the coannihilation/funnel region and in the focus-point region for $\tan\beta = 55$, but are smaller than those for $\tan\beta = 10$, especially in the focus-point region.

We see in Fig. 10 that the muon fluxes are quite insensitive to the value of $\Delta_s^{(p)}$ within the (plausible) range studied. On the other hand, Fig. 11 shows that the muon fluxes are more sensitive to the value of $\Sigma_{\pi N}$, particularly for $\tan\beta = 55$ and along the coannihilation strip for $\tan\beta = 10$ at larger $m_{1/2}$. The comparisons shown are for a threshold energy of 1 GeV, but similar conclusions apply for thresholds of 10 and 100 GeV (not shown). The value of $\Sigma_{\pi N}$ clearly impacts the ability of IceCube/DeepCore to detect $\tan\beta = 55$ models.
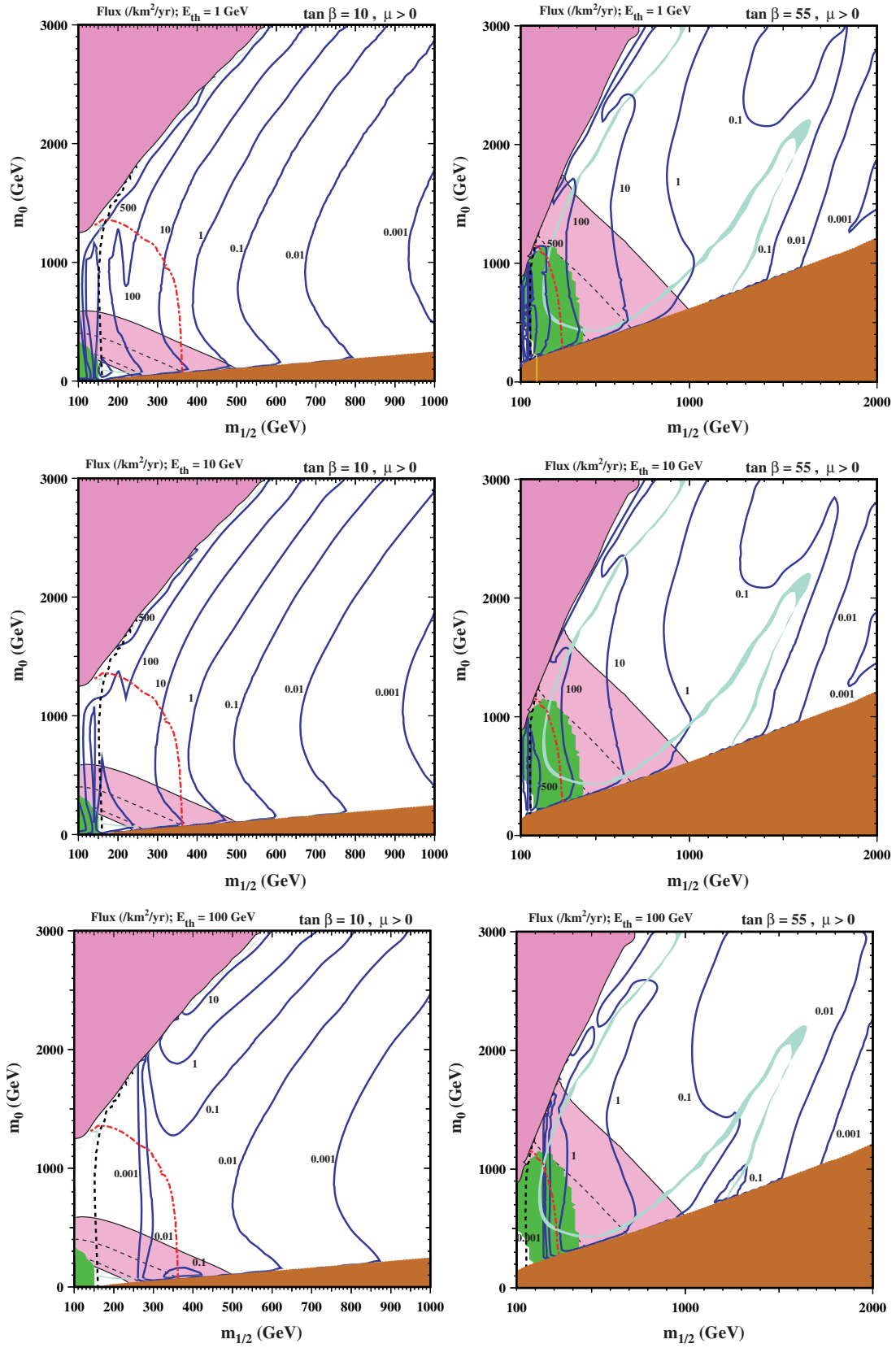
FIG. 8 (color online).   The $(m_{1/2}, m_0)$ planes for the CMSSM for $A_0 = 0$ and (left panels) $\tan\beta = 10$, (right panels) $\tan\beta = 55$ showing contours of the neutrino-induced muon flux through a detector with thresholds of 1 GeV (top row), 10 GeV (middle row), and 100 GeV (bottom row). Also shown are the theoretical, phenomenological, experimental, and cosmological constraints described in the text.
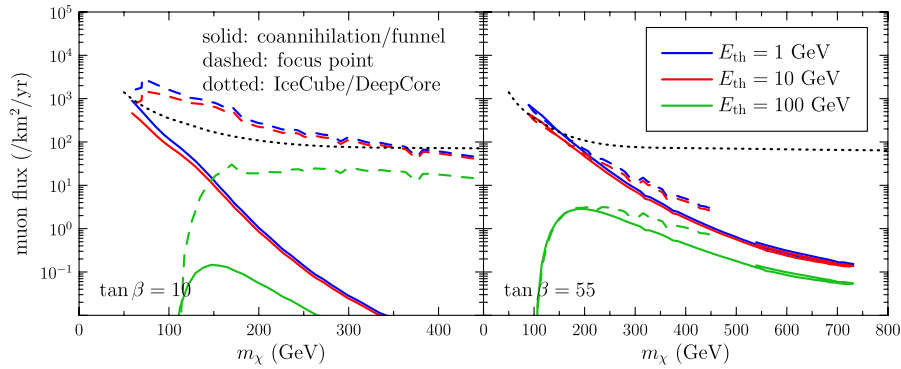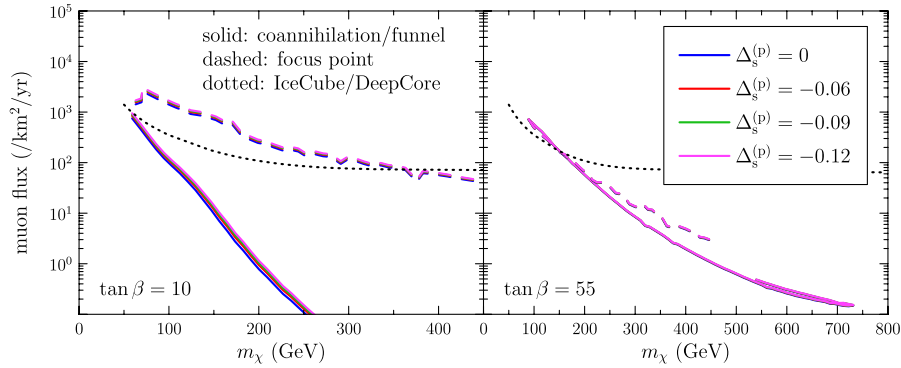
FIG. 9 (color online).    The CMSSM muon fluxes though a detector calculated for $A_0 = 0$ and (left panel) $\tan\beta = 10$, (right panel) $\tan\beta = 55$ along the WMAP strips in the coannihilation/funnel regions (solid lines) and the focus-point region (dashed lines). Fluxes are shown for muon energy thresholds of (top to bottom) 1 GeV, 10 GeV, and 100 GeV. Also shown is a conservative estimate of sensitivity of the IceCube/DeepCore detector (dotted lines), normalized to a muon threshold of 1 GeV, for a particular hard annihilation spectrum ($\tau\bar{\tau}$ for $m_\chi < 80$ GeV, $W^+W^-$ at higher masses). The IceCube/DeepCore sensitivity shown does not directly apply to the CMSSM flux curves, but can be treated as a rough approximation to which CMSSM models might be detectable, as discussed in the text.



FIG. 10 (color online).    (The CMSSM muon fluxes though a detector calculated for $A_0 = 0$ and (left panel) $\tan\beta = 10$, (right panel) $\tan\beta = 55$ along the WMAP strips in the coannihilation/funnel regions (solid lines) and the focus-point region (dashed lines). The fluxes are shown for $\Delta_s^{(p)}$ values of 0, $-0.06$, $-0.09$, and $-0.12$ with a detector threshold of 1 GeV. Also shown is a conservative approximation of sensitivity of the IceCube/DeepCore detector (dotted lines), as described in Fig. 9 and the text.
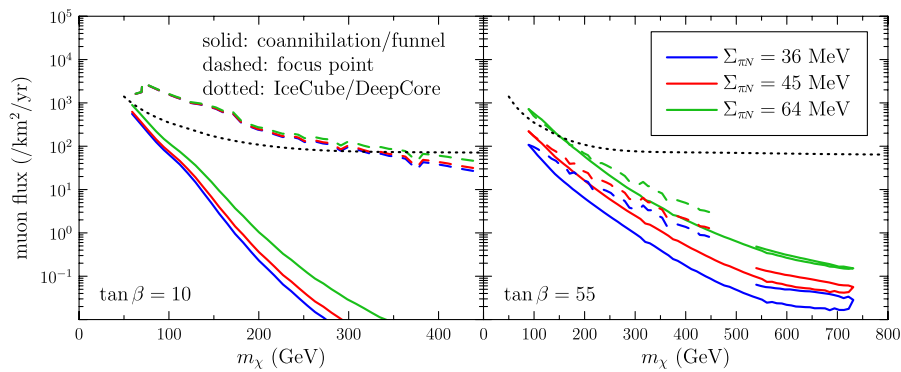


FIG. 11 (color online).    The CMSSM muon fluxes though a detector calculated for $A_0 = 0$ and (left panel) $\tan\beta = 10$, (right panel) $\tan\beta = 55$ along the WMAP strips in the coannihilation/funnel regions (solid lines) and the focus-point region (dashed lines). The fluxes are shown for $\Sigma_{\pi N}$ values of (top to bottom) 64, 45, and 36 MeV with a detector threshold of 1 GeV. Also shown is a conservative approximation of sensitivity of the IceCube/DeepCore detector (dotted lines), as described in Fig. 9 and the text.
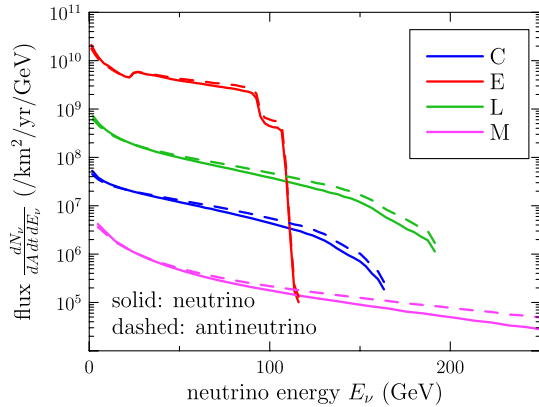
FIG. 12 (color online). The neutrino spectra in a terrestrial detector for (top to bottom) benchmark scenarios E, L, C, and M [13]. Neutrinos (solid lines) and antineutrinos (dashed lines) are shown separately.

### C. Fluxes for benchmark points

We now display complete spectra for the CMSSM benchmark scenarios C, E, L, and M of [13]. These are representative, respectively, of the low-mass region of the coannihilation strip, the focus-point region, the coannihilation region at larger $m_{1/2}$ and $\tan\beta$, and the rapid-annihilation funnel region. The benchmark parameters, capture/annihilation rates, and fluxes are given in Table II. Models E, L, and M are in or nearly in equilibrium between capture and annihilation, whereas model C is somewhat out of equilibrium.

The differential neutrino fluxes for these scenarios are shown in Fig. 12. The highest differential flux is found in model E, partly because it has a larger annihilation rate than the other models and partly because its neutrino spectrum is spread over a smaller range of energies (at 117 GeV, this model has the smallest LSP mass of the four). Model M has the lowest differential flux, but the spectrum is spread out over a wider range of energies; indeed, the spectrum for this model continues beyond the region shown. In all four models, the spectra end at the corresponding LSP mass. The plateau seen in model E arises from $W \rightarrow \mu\nu_\mu$ decays in the dominant $\chi\chi \rightarrow WW$ annihilation channel. Since the LSP mass is not much higher than the $W$ mass, the $W$s are produced with relatively low speeds. In this case, the neutrinos from the $W$ decays are kinematically limited to fall within the energy range corresponding to the plateau in the spectrum.

Figure 12 shows that the neutrino flux (solid lines) is slightly smaller than the antineutrino flux (dashed lines), particularly at higher energies. This arises from the higher neutral- and charged-current scattering cross sections for neutrinos, compared to antineutrinos, when passing through the Sun. The difference between neutrino and antineutrino fluxes grows more pronounced at higher energies. However, both neutrinos and antineutrinos are suppressed at higher energies, due to the increasing opacity
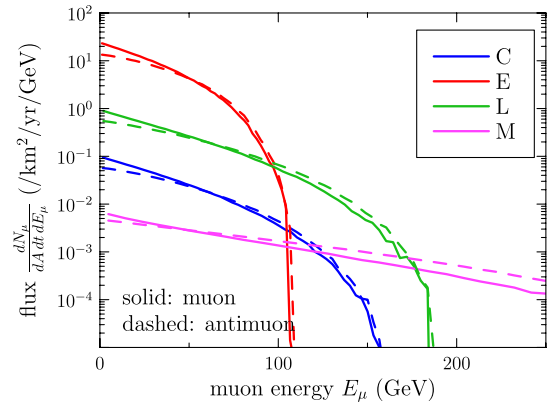


FIG. 13 (color online). The muon spectra in a terrestrial detector for (top to bottom) benchmark scenarios E, L, C, and M [13]. Muons (solid lines) and antimuons (dashed lines) are shown separately.

of the Sun: neutrinos are just more suppressed than antineutrinos.

Figure 13 shows the differential muon fluxes from these neutrino spectra. Model E still has the highest differential flux, but model M has increased relative to the other models over the intermediate energies shown in the figure, as compared to Fig. 12. This is because the higher-energy neutrinos in this model are capable of inducing additional muons at a range of lower energies.

While model E has the largest muon flux, it is all at relatively low energies that IceCube alone cannot detect. With a flux of just under $10^3/\text{km}^2/\text{yr}$ above 10 GeV (see Table II), however, its flux lies above the expected DeepCore detection level. Model L has the next highest spectrum, but would generate $\sim 50$ muons/km$^2$/yr above 10 GeV, probably falling just below the DeepCore detection level. However, its spectrum extends up to 190 GeV, yielding a significant flux above 100 GeV of 2.7/km$^2$/yr. While not high enough to be detected by IceCube alone, it is not far below the expected IceCube detection level either. The combination of DeepCore's low-energy sensitivity and IceCube's large volume make IceCube/DeepCore perhaps able to detect this model. Model M, while producing high-energy muons to which IceCube is most sensitive, has fluxes that are too low to be detected. Model C has neither the total flux nor an energy spectrum favorable for detection.

### VI. CONCLUSIONS

We have studied in detail the observability of muons produced by neutrinos and antineutrinos generated by the annihilations of CMSSM LSPs trapped inside the Sun, focusing, in particular, on models lying along the parameter strips where the relic LSP density falls within the range favored by WMAP [12].

For various reasons, discussed in Sec. V, it is not straightforward to apply direct detectability limits for

IceCube/DeepCore experiments on the CMSSM parameter space. The main complication is that the ability of the experiment to observe a signal above background depends on the shape of the neutrino spectrum. Nevertheless, a conservative estimation of the IceCube/DeepCore detectability limits can be made, that being $10^2$ to $10^3/km^2/yr$ for the muon flux above 1 GeV. Based on this, our conclusions are not very encouraging: along the coannihilation strips, we find that only models near the low-$m_{1/2}$ ends of the strips for $\tan\beta = 10$ and 55 may be detectable in IceCube/DeepCore. Nearly all of the focus-point strip may be detectable by IceCube/DeepCore for $\tan\beta = 10$; some of this strip may actually be detectable with the bulk (i.e. non-DeepCore) IceCube detector region alone. For $\tan\beta = 55$, IceCube/DeepCore will only be sensitive to the low-$m_{1/2}$ end of the focus-point region.

As for the benchmark scenarios, we find that model E (from the focus-point region) is expected to be detectable in IceCube/DeepCore, mainly due to the low-energy muon sensitivity of the DeepCore component as this model produces few high-energy muons that IceCube alone is sensitive to. On the other hand, the muon spectrum in model L (in the coannhilation region) extends to an energy of 190 GeV, and both the DeepCore and bulk IceCube components contribute to making this model borderline detectable. Model M (in the rapid-annihilation region), while also producing high-energy muons, produces too few to be detectable in IceCube/DeepCore, and model C (near the low-$m_{1/2}$ end of the coannihilation strip) has neither the flux nor the energy spectrum suitable for detection. These conclusions are quite robust with respect to uncertainties in the solar model. However, we do note that the calculated muon fluxes are quite sensitive to the assumed value of the $\pi$-nucleon $\sigma$ term $\Sigma_{\pi N}$, which controls the magnitude of spin-independent LSP scattering: we repeat our previous plea [17] to our experimental colleagues to reduce the uncertainty in $\Sigma_{\pi N}$.

These studies indicate that the indirect search for dark matter via annihilations that yield high-energy neutrinos and hence muons may not be the most promising way to discover supersymmetry, at least within the restrictive CMSSM framework. On the other hand, there are representative models where the calculated fluxes are close to the sensitivities of DeepCore and/or IceCube. Therefore, if other evidence for superymmetry were to be found, e.g., either at the LHC or in the direct search for dark matter scattering, it would be interesting to increase the sensitivities of DeepCore and IceCube, e.g., by decreasing the threshold or by increasing the effective surface area. *Une affaire à suivre!*

## ACKNOWLEDGMENTS

[1] M. W. Goodman and E. Witten, Phys. Rev. D **31**, 3059 (1985).

[2] J. Silk and M. Srednicki, Phys. Rev. Lett. **53**, 624 (1984); J. R. Ellis, R. A. Flores, K. Freese, S. Ritz, D. Seckel, and J. Silk, Phys. Lett. B **214**, 403 (1988); F. W. Stecker, S. Rudaz, and T. F. Walsh, Phys. Rev. Lett. **55**, 2622 (1985).

[3] P. Gondolo and J. Silk, Phys. Rev. Lett. **83**, 1719 (1999); G. Bertone, G. Sigl, and J. Silk, Mon. Not. R. Astron. Soc. **337**, 98 (2002); G. Bertone, E. Nezri, J. Orloff, and J. Silk, Phys. Rev. D **70**, 063503 (2004).

[4] J. Silk, K. A. Olive, and M. Srednicki, Phys. Rev. Lett. **55**, 257 (1985); M. Srednicki, K. A. Olive, and J. Silk, Nucl. Phys. **B279**, 804 (1987); J. S. Hagelin, K. W. Ng, and K. A. Olive, Phys. Lett. B **180**, 375 (1986); K. W. Ng, K. A. Olive, and M. Srednicki, Phys. Lett. B **188**, 138 (1987); T. K. Gaisser, G. Steigman, and S. Tilav, Phys. Rev. D **34**, 2206 (1986); F. Halzen, T. Stelzer, and M. Kamionkowski, Phys. Rev. D **45**, 4439 (1992); L. Bergstrom, J. Edsjo, and P. Gondolo, Phys. Rev. D **55**, 1765 (1997); K. Freese and M. Kamionkowski, Phys. Rev. D **55**, 1771 (1997).

[5] K. Freese, Phys. Lett. **167B**, 295 (1986); L. M. Krauss, M. Srednicki, and F. Wilczek, Phys. Rev. D **33**, 2079 (1986).

[6] N. W. Evans, F. Ferrer, and S. Sarkar, Phys. Rev. D **69**, 123501 (2004); L. Pieri, A. Pizzella, E. M. Corsini, E. D. Bontá, and F. Bertola, Astron. Astrophys. **496**, 351 (2009); M. Kuhlen, arXiv:0906.1822.

[7] S. Colafrancesco and B. Mele, Astrophys. J. **562**, 24 (2001); S. Colafrancesco, Astron. Astrophys. **422**, L23 (2004); S. Colafrancesco, S. Profumo, and P. Ullio, Astron. Astrophys. **455**, 21 (2006); S. Profumo, Phys. Rev. D **77**, 103510 (2008); Q. Yuan, X. Bi, F. Huang, and X. Chen, J. Cosmol. Astropart. Phys. 10 (2009) 013; J. Lavalle, C. Boehm, and J. Barthes, arXiv:0907.5589.

[8] A. Corsetti and P. Nath, Int. J. Mod. Phys. A **15**, 905 (2000); J. L. Feng, K. T. Matchev, and F. Wilczek, Phys. Rev. D **63**, 045024 (2001); V. D. Barger, F. Halzen, D. Hooper, and C. Kao, Phys. Rev. D **65**, 075022 (2002); H. Baer, A. Belyaev, T. Krupovnickas, and J. O'Farrill, J. Cosmol. Astropart. Phys. 08 (2004) 005; R. Trotta, R. R. de Austri, and C. P. d. Heros, J. Cosmol. Astropart. Phys.

08 (2009) 034.

[9] M. Drees and M. M. Nojiri, Phys. Rev. D **47**, 376 (1993); H. Baer and M. Brhlik, Phys. Rev. D **53**, 597 (1996); **57**, 567 (1998); V. D. Barger and C. Kao, Phys. Rev. D **57**, 3131 (1998); J. R. Ellis, T. Falk, G. Ganis, K. A. Olive, and M. Srednicki, Phys. Lett. B **510**, 236 (2001); V. D. Barger and C. Kao, Phys. Lett. B **518**, 117 (2001); L. Roszkowski, R. Ruiz de Austri, and T. Nihei, J. High Energy Phys. 08 (2001) 024; A. B. Lahanas and V. C. Spanos, Eur. Phys. J. C **23**, 185 (2002); A. Djouadi, M. Drees, and J. L. Kneur, J. High Energy Phys. 08 (2001) 055; U. Chattopadhyay, A. Corsetti, and P. Nath, Phys. Rev. D **66**, 035003 (2002); J. R. Ellis, K. A. Olive, and Y. Santoso, New J. Phys. **4**, 32 (2002); H. Baer, C. Balazs, A. Belyaev, J. K. Mizukoshi, X. Tata, and Y. Wang, J. High Energy Phys. 07 (2002) 050; R. Arnowitt and B. Dutta, arXiv:hep-ph/0211417.

[10] J. R. Ellis, K. A. Olive, Y. Santoso, and V. C. Spanos, Phys. Lett. B **565**, 176 (2003).

[11] H. Baer and C. Balazs, J. Cosmol. Astropart. Phys. 05 (2003) 006; A. B. Lahanas and D. V. Nanopoulos, Phys. Lett. B **568**, 55 (2003); U. Chattopadhyay, A. Corsetti, and P. Nath, Phys. Rev. D **68**, 035005 (2003); C. Munoz, Int. J. Mod. Phys. A **19**, 3093 (2004); R. L. Arnowitt, B. Dutta, and B. Hu, arXiv:hep-ph/0310103.

[12] E. Komatsu *et al.* (WMAP Collaboration), Astrophys. J. Suppl. Ser. **180**, 330 (2009).

[13] M. Battaglia *et al.*, Eur. Phys. J. C **22**, 535 (2001); M. Battaglia, A. De Roeck, J. R. Ellis, F. Gianotti, K. A. Olive, and L. Pape, Eur. Phys. J. C **33**, 273 (2004); A. De Roeck, J. R. Ellis, F. Gianotti, F. Moortgat, K. A. Olive, and L. Pape, Eur. Phys. J. C **49**, 1041 (2007).

[14] A. Bottino, F. Donato, N. Fornengo, and S. Scopel, Astropart. Phys. **13**, 215 (2000).

[15] E. Accomando, R. L. Arnowitt, B. Dutta, and Y. Santoso, Nucl. Phys. **B585**, 124 (2000).

[16] J. R. Ellis, K. A. Olive, Y. Santoso, and V. C. Spanos, Phys. Rev. D **71**, 095007 (2005).

[17] J. R. Ellis, K. A. Olive, and C. Savage, Phys. Rev. D **77**, 065026 (2008).

[18] V. Niro, A. Bottino, N. Fornengo, and S. Scopel, Phys. Rev. D **80**, 095019 (2009).

[19] M. Alekseev *et al.* (COMPASS Collaboration), arXiv:0707.4077.

[20] A. Airapetian *et al.* (HERMES Collaboration), Phys. Lett. B **666**, 446 (2008).

[21] M. M. Pavan, I. I. Strakovsky, R. L. Workman, and R. A. Arndt, PiN Newslett. **16**, 110 (2002).

[22] R. D. Young and A. W. Thomas, arXiv:0901.3310.

[23] J. Giedt, A. W. Thomas, and R. D. Young, arXiv:0907.4177.

[24] J. Ahrens *et al.* (IceCube Collaboration), Astropart. Phys. **20**, 507 (2004).

[25] C. Wiebusch and f. t. I. Collaboration, arXiv:0907.2263.

[26] O. Buchmueller *et al.*, J. High Energy Phys. 09 (2008) 117; Eur. Phys. J. C **64**, 391 (2009).

[27] Joint LEP 2 Supersymmetry Working Group, "Combined LEP Chargino Results, up to 208 GeV," http://lepsusy.web.cern.ch/lepsusy/www/inos_moriond01/charginos_pub.html.

[28] R. Barate *et al.* (ALEPH, DELPHI, L3, OPAL Collaborations: the LEP Working Group for Higgs boson searches), Phys. Lett. B **565**, 61 (2003); D. Zer-Zion, *Proceedings of the 32nd International Conference on High-Energy Physics (ICHEP 04), Beijing, China, 2004* (World Scientific, Hackensack, 2004); Report Nos. LHWG-NOTE-2004-01, ALEPH-2004-008, DELPHI-2004-042, L3-NOTE-2820, OPAL-TN-744, http://lephiggs.web.cern.ch/LEPHIGGS/papers/August2004_MSSM/index.html.

[29] S. Heinemeyer, W. Hollik, and G. Weiglein, Comput. Phys. Commun. **124**, 76 (2000); Eur. Phys. J. C **9**, 343 (1999); G. Degrassi, S. Heinemeyer, W. Hollik, P. Slavich, and G. Weiglein, Eur. Phys. J. C **28**, 133 (2003); M. Frank, T. Hahn, S. Heinemeyer, W. Hollik, H. Rzehak, and G. Weiglein, J. High Energy Phys. 02 (2007) 047; http://www.feynhiggs.de/.

[30] S. Chen *et al.* (CLEO Collaboration), Phys. Rev. Lett. **87**, 251807 (2001); P. Koppenburg *et al.* (Belle Collaboration), Phys. Rev. Lett. **93**, 061803 (2004); B. Aubert *et al.* (*BABAR* Collaboration), arXiv:hep-ex/0207076; E. Barberio *et al.* (Heavy Flavor Averaging Group (HFAG)), arXiv:hep-ex/0603003.

[31] G. W. Bennett *et al.* (Muon G-2 Collaboration), Phys. Rev. D **73**, 072003 (2006).

[32] B. Aubert *et al.* (*BABAR* Collaboration), Phys. Rev. Lett. **103**, 231801 (2009).

[33] M. Davier, A. Hoecker, B. Malaescu, C. Z. Yuan, and Z. Zhang, arXiv:0908.4300.

[34] K. Freese, J. A. Frieman, and A. Gould, Phys. Rev. D **37**, 3388 (1988).

[35] A. Serenelli, S. Basu, J. W. Ferguson, and M. Asplund, arXiv:0909.2668.

[36] M. Asplund, N. Grevesse, A. J. Sauval, and P. Scott, Annu. Rev. Astron. Astrophys. **47**, 481 (2009).

[37] A. Gould, Astrophys. J. **321**, 571 (1987).

[38] A. Gould, Astrophys. J. **388**, 338 (1992).

[39] P. F. Smith and J. D. Lewin, Phys. Rep. **187**, 203 (1990); J. D. Lewin and P. F. Smith, Astropart. Phys. **6**, 87 (1996).

[40] G. Duda, A. Kemper, and P. Gondolo, J. Cosmol. Astropart. Phys. 04 (2007) 012.

[41] A. Gould, Astrophys. J. **321**, 560 (1987).

[42] C. Savage, The Dark Side of the Universe 2007, Minneapolis, Minnesota, 2007.

[43] A. H. G. Peter, Phys. Rev. D **79**, 103532 (2009).

[44] N. Grevesse and A. J. Sauval, Space Sci. Rev. **85**, 161 (1998).

[45] A. M. Serenelli, arXiv:0910.3690.

[46] P. Gondolo, J. Edsjo, P. Ullio, L. Bergstrom, M. Schelke, and E. A. Baltz, J. Cosmol. Astropart. Phys. 07 (2004) 008; P. Gondolo, J. Edsjo, P. Ullio, L. Bergstrom, M. Schelke, E. A. Baltz, T. Bringmann, and G. Duda, http://www.physto.se/~edsjo/darksusy/.

[47] H. Leutwyler, Phys. Lett. B **378**, 313 (1996).

[48] C. Amsler *et al.* (Particle Data Group), Phys. Lett. B **667**, 1 (2008), and 2009 partial update for the 2010 edition available on the PDG WWW pages (http://pdg.lbl.gov/).

[49] Tevatron Electroweak Working Group, CDF, and D0 Collaborations, arXiv:0903.2503.

[50] B. Borasoy and U. G. Meissner, Ann. Phys. (N.Y.) **254**, 192 (1997).

[51] Y. Goto *et al.* (Asymmetry Analysis Collaboration), Phys. Rev. D **62**, 034017 (2000).

[52] E. Leader, A. V. Sidorov, and D. B. Stamenov, Phys. Rev. D **67**, 074017 (2003).

[53] V. A. Bednyakov and F. Simkovic, Fiz. Elem. Chastits At. Yadra **36**, 257 (2005) [Phys. Part. Nucl. **36**, 131 (2005)].

[54] M. A. Shifman, A. I. Vainshtein, and V. I. Zakharov, Phys. Lett. **78B**, 443 (1978).

[55] A. I. Vainshtein, V. I. Zakharov, and M. A. Shifman, Usp. Fiz. Nauk **131**, 537 (1980) [Sov. Phys. Usp. **23**, 429 (1980)].

[56] H. Y. Cheng, Phys. Lett. B **219**, 347 (1989).

[57] J. R. Ellis, A. Ferstl, and K. A. Olive, Phys. Lett. B **481**, 304 (2000); Phys. Rev. D **63**, 065016 (2001); Phys. Lett. B **532**, 318 (2002).

[58] J. Gasser, H. Leutwyler, and M. E. Sainio, Phys. Lett. B **253**, 252 (1991).

[59] M. Knecht, PiN Newslett. **15**, 108 (1999).

[60] M. E. Sainio, PiN Newslett. **16**, 138 (2002).

[61] S. Ritz and D. Seckel, Nucl. Phys. **B304**, 877 (1988).

[62] G. F. Giudice and E. Roulet, Nucl. Phys. **B316**, 429 (1989).

[63] J. Edsjo, Diploma thesis, Uppsala University [Report No. TSL/ISV-93-0091 (ISSN 0284-2769)].

[64] G. Jungman and M. Kamionkowski, Phys. Rev. D **51**, 328 (1995).

[65] J. R. Ellis, R. A. Flores, and S. S. Masood, Phys. Lett. B **294**, 229 (1992).

[66] M. Blennow, J. Edsjo, and T. Ohlsson, J. Cosmol. Astropart. Phys. 01 (2008) 021; J. Edsjo, WimpSim Neutrino Monte Carlo, http://www.physto.se/~edsjo/wimpsim/.

[67] M. Cirelli, N. Fornengo, T. Montaruli, I. Sokalski, A. Strumia, and F. Vissani, Nucl. Phys. **B727**, 99 (2005); **B790**, 338(E) (2008); http://www.marcocirelli.net/DMnu.html.

[68] E. Resconi *et al.*, IceCube Collaboration, Nucl. Instrum. Methods Phys. Res., Sect. A **602**, 7 (2009).

[69] R. Abbasi *et al.* (IceCube Collaboration), Phys. Rev. Lett. **102**, 201302 (2009). The combined IceCube/DeepCore flux sensitivities are only found in Fig. 3 of the arXiv version 2.

[70] G. Ingelman and M. Thunman, Phys. Rev. D **54**, 4385 (1996).